ARL-TR-10486 ● Nov 2026

Numerical Investigation of Control Pin Aerodynamics for Pitch and Roll Control of a High-Speed Vehicle

by Jubaraj Sahu and Justin Paul

DISTRIBUTION STATEMENT A. Approved for public release: distribution unlimited.

NOTICES

Disclaimers

The findings in this report are not to be construed as an official Department of the Army position unless so designated by other authorized documents.

Citation of manufacturer's or trade names does not constitute an official endorsement or approval of the use thereof.

Destroy this report when it is no longer needed. Do not return it to the originator.

This work was supported in part by a grant of high-performance computing time from the U.S. Department of Defense High-Performance Computing Modernization Program.

ARL-TR-10486 ● Nov 2026





Numerical Investigation of Control Pin Aerodynamics for Pitch and Roll Control of a High-Speed Vehicle

Jubaraj Sahu
SURVICE Engineering Company

Justin Paul
DEVCOM Army Research Laboratory

DISTRIBUTION STATEMENT A. Approved for public release: distribution unlimited.

REPORT DOCUMENTATION PAGE

1. REPORT DATE	2. REPORT TYPE	3. DATES COVERED	
		START DATE	END DATE
November 2026	Technical Report	10 July 2025	20 July 2026

4. TITLE AND SUBTITLE
Numerical Investigation of Control Pin Aerodynamics for Pitch and Roll Control of a High-Speed Vehicle

5a. CONTRACT NUMBER	5b. GRANT NUMBER	5c. PROGRAM ELEMENT NUMBER
5d. PROJECT NUMBER 622141.DN6.04	**5e. TASK NUMBER**	**5f. WORK UNIT NUMBER**

6. AUTHOR(S)
Jubaraj Sahu and Justin Paul

7. PERFORMING ORGANIZATION NAME(S) AND ADDRESS(ES)	8. PERFORMING ORGANIZATION REPORT NUMBER
DEVCOM Army Research Laboratory ATTN: FCDD-RLA-WD Aberdeen Proving Ground, MD 21005	ARL-TR-10486

9. SPONSORING/MONITORING AGENCY NAME(S) AND ADDRESS(ES)	10. SPONSOR/MONITOR'S ACRONYM(S)	11. SPONSOR/MONITOR'S REPORT NUMBER(S)

12. DISTRIBUTION/AVAILABILITY STATEMENT
DISTRIBUTION STATEMENT A. Approved for public release: distribution unlimited.

13. SUPPLEMENTARY NOTES
ORCID: Jubaraj Sahu, 0000-0003-3347-4387

14. ABSTRACT
Pin effectors in the shape of rectangular prisms were numerically investigated for roll and pitch control of a generic high-speed test vehicle at Mach 3 over a range of angles of attack (α), using both Euler and Navier–Stokes methods. A baseline, no-pin configuration was simulated using both methodologies to obtain nominal aerodynamic performance. For pitch control, five variant configurations using one to three pins were simulated and analyzed. For roll control, three additional configurations with four pin effectors were considered. The performance of the pin effector configurations was determined from both Euler and Navier–Stokes solutions. For pitch control, both simulation methods showed the variant configurations maintained appreciable fractions of change in pitching moment coefficient generated by the pin effectors at high α, demonstrating the pin effectors maintain reasonable effectiveness on the lee side in the shadow of the vehicle. The aerodynamic performance of the variant configurations demonstrated nonlinear trends in comparison with the baseline configuration. Generally, comparisons between Euler and Navier–Stokes solutions show good agreement. For roll control, inherent flow interactions and asymmetric flow patterns makes roll moment predictions more difficult. The Euler method overpredicts the roll moment, is less reliable compared with Navier–Stokes, and may not be suitable for prediction of roll control.

15. SUBJECT TERMS
Weapons Sciences, control pin, computational fluid dynamics, CFD, Navier–Stokes, Euler, pitch control, roll control

16. SECURITY CLASSIFICATION OF:			17. LIMITATION OF ABSTRACT	18. NUMBER OF PAGES
a. REPORT	b. ABSTRACT	C. THIS PAGE		
UNCLASSIFIED	UNCLASSIFIED	UNCLASSIFIED	UU	60

19a. NAME OF RESPONSIBLE PERSON	19b. PHONE NUMBER *(Include area code)*
Jubaraj Sahu	(520) 691-4814

STANDARD FORM 298 (REV. 5/2020)
Prescribed by ANSI Std. Z39.18

Contents

List of Figures iv

List of Tables vii

Acknowledgments viii

1. Introduction 1

2. Geometry Definition 4

3. Methodologies 7

3.1 Euler CFD Software: Cart3D 7

3.2 Navier–Stokes CFD code: CFD^{++} 10

4. Results 12

4.1 Pitch Control Simulations 12

4.1.1 Flow-Field Analysis 13

4.1.2 Aerodynamic Performance 24

4.2 Roll Control Simulations 31

4.2.1 Surface Pressure Contour Analysis 31

4.2.2 Aerodynamic Roll Performance 35

5. Conclusions 42

6. References 44

Nomenclature 48

List of Symbols, Abbreviations, and Acronyms 49

Distribution List 50

List of Figures

Figure 1. Flight vehicle with pin effectors symmetric on the lee side of the vehicle. The full projectile is shown on the left and a close-up view is shown on the right. 5

Figure 2. Conceptual diagrams (not to scale) of configurations analyzed. 6

Figure 3. Computational model, y-z plane looking from the nose and showing the four-pin, 27° roll (left), and the four-pin, 33° (right) roll configurations, 0.126-cal. height. 6

Figure 4. Example pitch plane mesh view. 8

Figure 5. Detailed views of the mesh in the region of the pin effector of the one-pin configuration. 8

Figure 6. Detailed views of the mesh in the region of the pin effector of the two-pin, 27° configuration. 9

Figure 7. Detailed views of the mesh in the region of the pin effector of the two-pin, 33° configuration. 9

Figure 8. Detailed views of the mesh in the region of the pin effector of the three-pin, 13.2-mm configuration. 9

Figure 9. Detailed views of the mesh in the region of the pin effector of the three-pin, 8.8-mm configuration. 9

Figure 10. Computational model, x-z plane (left) and y-z plane (right) showing the two-pin, 27° configuration. 10

Figure 11. Computational mesh expanded near the body. 11

Figure 12. Computational mesh at a cross section through the fins (past the pins). 12

Figure 13. Computational body surface mesh and pin effector meshes (left) with holes cut by the pin effector on the body (right). 12

Figure 14. Mach and C_p contours of the Euler simulations for the one-pin configuration as viewed from the side (left) and the top (right) at α = –15° (top), α = 0° (middle), and α = 15° (bottom). 13

Figure 15. Mach and C_p contours of the Euler simulations for the two-pin, 27° configuration as viewed from the side (left) and the top (right) at α = –15° (top), α = 0° (middle), and α = 15° (bottom). 14

Figure 16. Mach and C_p contours of the Euler simulations for the three-pin, 13.2-mm configuration as viewed from the side (left) and the top (right) at α = –15° (top), α = 0° (middle), and α = 15° (bottom). 15

Figure 17 Lee side and wind side Euler surface pressure of the two-pin, 27° configuration at α = 0°. 16

Figure 18. Surface pressure contours showing detail near the pin effectors for Euler simulations (top four rows) and RANS simulations (bottom four

rows) comparing the one-pin, two-pin, 27°, and three-pin, 13.2-mm configurations at selected positive α from $\alpha = 0°$ to $\alpha = 15°$. 17

Figure 19. Surface pressure contours showing detail near the pin effectors for Euler simulations (top four rows) and RANS simulations (bottom four rows) comparing the one-pin, two-pin, 27°, and three-pin, 13.2-mm configurations at selected negative α from $\alpha = –15°$ to $\alpha = 0°$. 18

Figure 20. Surface pressure contours showing detail near the pin effectors for RANS simulations comparing the two-pin, 27°, and two-pin, 33° configurations at selected positive α from $\alpha = 0°$ to $\alpha = 15°$. 20

Figure 21. Surface pressure contours showing detail near the pin effectors for RANS simulations comparing the two-pin, 27°, and two-pin, 33° configurations at selected negative α from $\alpha = –15°$ to $\alpha = 0°$. 21

Figure 22. Surface pressure contours showing detail near the pin effectors for RANS simulations comparing the three-pin, 13.2-mm, and three-pin, 8.8-mm configurations at selected positive α from $\alpha = 0°$ to $\alpha = 15°$. 22

Figure 23. Surface pressure contours showing detail near the pin effectors for RANS simulations comparing the three-pin, 13.2-mm, and three-pin, 8.8-mm configurations at selected negative α from $\alpha = –15°$ to $\alpha = 0°$. 23

Figure 24. C_N calculated from RANS (a) and Euler (b) simulations for the one-pin, two-pin, 27°, and three-pin, 13.2-mm configurations; and for the two-pin (c) and three-pin configurations (d)..... 25

Figure 25. ΔC_N calculated from RANS and Euler simulations for the one-pin, two-pin, 27°, and three-pin, 13.2-mm configurations (left), the two, 2-pin configurations (middle) and the two, 3-pin configurations (right). 25

Figure 26. C_m calculated from RANS (a) and Euler (b) simulations for the one-pin, two-pin, 27°, and three-pin, 13.2-mm configurations; and for the two-pin (c) and three-pin configurations (d)..... 26

Figure 27. ΔC_m calculated from RANS and Euler simulations for the one-pin, two-pin, 27°, and three-pin, 13.2-mm configurations (left); the two, 2-pin configurations (middle); and the two, 3-pin configurations (right). 26

Figure 28. C_A calculated from RANS (a) and Euler (b) simulations for the one-pin, two-pin, 27°, and three-pin, 13.2-mm configurations; and for the two-pin (c) and three-pin configurations (d)..... 27

Figure 29. ΔC_A calculated from RANS and Euler simulations for the one-pin, two-pin, 27°, and three-pin, 13.2-mm configurations (left); the two, 2-pin configurations (middle); and the two, 3-pin configurations (right). 27

Figure 30. Equivalent tail-flap deflection for $\alpha = 0°$ calculated using C_N and C_m for four pin effector configurations (two-pin, 33° excluded). The top row compares RANS and Euler results for the one-pin, two-pin, 27°,

three-pin, 13.2-mm configurations; and the bottom row compares the two 3-pin configurations with different heights..... 30

Figure 31. Computed surface pressure contours showing detail near the pin effectors from RANS simulations for the four-pin, 27° roll configuration at α = 0°, x-z view. 32

Figure 32. Computed surface pressure contours showing detail near the pin effectors from RANS simulations for the four-pin, 27° roll configuration at α = 5°, x-y view from top, lee side (left) and x-y view from bottom, wind side (right). 32

Figure 33. Computed surface pressure contours showing detail near the pin effectors from RANS simulations for the four-pin, 27° roll configuration at α = 5°, x-z or side view (left) and x-z side view rotated 180° (right)..... 32

Figure 34. Computed surface pressure contours showing detail near the pin effectors from RANS simulations for the four-pin, 27° roll configuration at α = 8°, x-y view from top, lee side (left) and x-y view from bottom, wind side (right). 33

Figure 35. Computed surface pressure contours showing detail near the pin effectors from RANS simulations for the four-pin, 27° roll configuration at α = 8°, x-z or side view (left) and x-z side view rotated 180° (right)..... 33

Figure 36. Computed surface pressure contours showing detail near the pin effectors from Euler simulations for the four-pin, 27° roll configuration at α = 0°, x-z view. 34

Figure 37. Computed surface pressure contours showing detail near the pin effectors from Euler simulations for the four-pin, 27° roll configuration at α = 5°, x-z or side view (left), and x-z side view rotated 180° (right)..... 34

Figure 38. Computed surface pressure contours showing detail near the pin effectors from Euler simulations for the four-pin, 27° roll configuration at α = 8°, x-z or side view (left), and x-z side view rotated 180° (right)..... 34

Figure 39. Computed surface pressure contours on the lee side showing detail near the pin effectors for the four-pin, 27° roll configuration at α = 5°, RANS (left) and Euler (right). 35

Figure 40. Computed surface pressure contours on the lee side showing detail near the pin effectors for the four-pin, 27° roll configuration at α = 8°, RANS (left) and Euler (right). 35

Figure 41. Comparison of computed C_A from RANS and Euler simulations for the four-pin, 27°, the four-pin, 33°, 0.126-cal. (tall) roll configurations.. 36

Figure 42. Comparison of computed C_S from RANS and Euler simulations for the four-pin, 33°, 0.126-cal. (tall) roll configurations. 37

Figure 43. Comparison of computed C_N from RANS and Euler simulations for the four-pin, 33°, 0.126-cal. (tall) roll configurations. 37

Figure 44. Comparison of computed C_l from RANS and Euler simulations for the four-pin, 27°, the four-pin, 33°, 0.126-cal. (tall) roll configurations.. 39

Figure 45. Comparison of computed C_m from RANS and Euler simulations for the four-pin, 27°, the four-pin, 33°, 0.126-cal. (tall) roll configurations. 40

Figure 46. Comparison of computed C_n from RANS and Euler simulations for the four-pin, 27°, the four-pin, 33°, 0.126-cal. (tall) roll configurations.. 40

List of Tables

Table 1. Details of body component contributions to the roll moment coefficient, C_l, from RANS simulations for the 0.126-cal. (tall), four-pin, 27° roll configuration as a function of angle of attack. 41

Acknowledgments

We thank Dr. James DeSpirito (ARL) for providing expert advice and analysis in discussions of the results and for his help planning the approach of this investigation. We also sincerely thank Dr. Sidra Siton (ARL) for a very thorough review of this report and her constructive comments.

1. Introduction

Control forces and moments provide the control authority required for pitch and roll control of a projectile. Either active or passive means can be used to generate required control forces and moments during flight. Flow control generally produces more complex flow fields with shock-/boundary-layer interactions and viscous-dominated separated flow regions, which in turn make accurate determination of aerodynamics more challenging. Traditionally, canards[1–6] and rear-fins (or flaps)[7–9] are used for projectile control maneuvers. Canards have been used to provide control forces and moments for maneuvering projectiles successfully at both subsonic and supersonic speeds. However, a major concern with canards is that adverse flow interactions can occur downstream on the body that vary with flow condition, angle of attack, and canard deflection. These flow interactions must be accounted for in the computations and design analyses of canard-controlled projectiles. Rear-fins or flaps can also be used to generate control forces/moments while minimizing adverse flow interactions compared with canard control.

In the early 2000s and into the 2010s, other control mechanisms—deployable pins[10–16] and microflaps[17–26]—were investigated for their feasibility in providing control forces and moments for projectile control. As opposed to pins that have generally circular cross sections, microflaps are similar, but have rectangular or square cross sections. These "pin-based" control effectors have been both experimentally and numerically studied to better understand how they could be used to guide supersonic projectiles. In this case, flow control is achieved by locating the small pins/microflaps between fins of the fin-stabilized projectile. The location of the pins/microflaps in the rear or aft-end of the body offers an advantage in that it may minimize adverse flow-interaction effects commonly associated with canard and jet control[27–29] because of their usual upstream location. At supersonic speeds, the pins/microflaps alter the flow field in the finned region of the projectile containing the flow effectors due to complex shock-boundary-layer interactions and shock-wave interactions among the body, fins, and pins/microflaps. These flow interactions result in asymmetric pressure distribution over the rear finned section, producing forces and moments for projectile control.

Initially, a number of investigations were conducted both at Georgia Tech Research Institute (GTRI) and U.S. Army Combat Capabilities Development Command (DEVCOM) Army Research Laboratory (ARL) to determine if pin-based actuators could be strategically placed to provide the control force required to turn or steer a projectile.[10–12] Massey et al.[10] studied the effect of pin-based actuators for control of a projectile at supersonic speeds. Masey et al.[11] performed a series of 6 degrees-

of-freedom (6DOF) simulations and flight tested the projectile with pins to determine the feasibility of these actuators to guide a projectile at $M = 2$ and $M = 3$. Further testing was conducted by Massey and Silton[12] to divert a projectile at $M = 4$. Silton and Massey[13] used an integrated computational and flight test approach to demonstrate the ability of diametrically opposed pins to produce a roll torque. Analysis of both the flight test data and simulations showed that the projectile with pins developed the expected rolling moments. To further evaluate the pin concept for directional control, a series of experiments and computational studies was conducted by Massey et al.[14] and Massey and Silton.[15] The wind tunnel tests conducted at GTRI provided insight for best placement of the actuators for high levels of control forces. Predicted control forces were found to be in close agreement with the experimental measurements. Based on the computational fluid dynamics (CFD) and 6DOF analyses, the projectile with the pins was flight tested at ARL. The flight tests demonstrated the performance of the pins for roll control of a supersonic projectile with results used to validate computational predictions. Larger roll moment was found with a longer pin compared with a short pin. All these studies clearly indicated the viability or potential of pin-based actuators for directional control (pitch or roll) at supersonic speeds using two pins. Another investigation by Bell et al.[16] followed the work at GTRI and computationally studied the interaction effect of a local protuberance (i.e., a pin) with the fin of a supersonic projectile providing more insight into the flow physics.

Work continued into the 2010s with similar approaches of analyzing effectiveness using CFD simulations and coupled CFD/rigid-body dynamics (RBD) flyout trajectory simulations.[17–23] These studies focused on a set of microflaps as the flow control mechanism and was investigated for feasibility of providing adequate aerodynamic control. Computed control forces and moments generated by the microflaps were used in a 6DOF flight dynamic analysis to demonstrate cross-range control of the finned projectile. These pin effectors were analyzed in a variety of ways, such as comparing configurations for better cross-range metrics and analyzing mechanical feasibility while attempting to transform the pressure distribution over stabilizing control surfaces.

Cler et al.[17] and Dykes et al.[18] used a flat-plate fin interaction design-of-experiments model to examine the control authority at $M = 1.7$ and obtained an optimized layout with four microflaps. Sahu and Heavey[19] computationally studied the effect of microflaps on the aerodynamics of a finned projectile using the same set of four microflaps from $M = 0.8$ to $M = 4.0$. Computed results indicated that the microflaps were effective only at supersonic speeds, not at transonic speeds. There were no shocks generated by the pins at $M = 0.9$, but strong shocks were generated by the pins at higher speeds ($M > 1.2$). Formation of these shocks and their interaction on

the fins result in the pins being effective at supersonic speeds. Scheuermann et al.[20] conducted a combined computational and experimental flight test study and provided aerodynamic characterization results. Resulting aerodynamic models were found to generally be in good agreement. This work continued to show promise for microflaps as a viable control mechanism at supersonic speeds, ($2 < M < 3$). Sahu[21] reported initial optimization results based on the change in normal force for a finned configuration with six and eight microflaps. These optimization efforts were continued by Sahu[22] with a focus on how to generate maximum control authority on a finned projectile configuration. This detailed study investigated geometric parameters, microflap locations, and the number of microflaps that are used to maximize the control authority generated by the flaps. This work clearly showed superior performance of the 6- and 8-microflap configurations producing much larger control forces—up to 21 newtons more—than that produced by the baseline 4-flap configuration. It also investigated the flow control performance and the effectiveness of the optimized eight-microflap configuration at various speeds up to $M = 5$.

Further research was carried out in a comprehensive computational study by Leonard et al.,[23] exploring the design space of microspoiler or microflap (names used interchangeably) configurations to maximize the control authority through optimization of microspoiler arrangement, height, and placement on the projectile. CFD computations were performed for prediction of control forces and moments throughout a wide range of Mach numbers from $M = 1.1$ to $M = 5.0$. The 6DOF simulations predicted almost twice the control authority for the optimized configuration compared with previous studies.[18,20] The results also showed that the optimized microspoiler geometry exhibited almost the same level of control authority exhibited by canard control mechanism. Additionally, this research provided further insight into the control amplification caused by the rear fins by comparing CFD predicted control forces with and without fins (i.e., spin-stabilized) from $M = 1.1$ to $M = 5.0$. Computed results showed that the fins amplify the control effectiveness of the microflaps by approximately a factor of two while increasing drag by a negligible amount. The computed results also support the possibility that the microflaps could provide control authority on spin-stabilized projectiles. An example of such application of a microspoiler to a spin-stabilized projectile has recently been reported by Chang and Li.[26] The optimized eight-microflap concept[22,23] formed the basis for the design and flight testing of a projectile at ARL. Actual electromechanical actuator design used for testing the projectile guidance with pin is reported by Celmins.[24] A series of test projectiles were created with an integrated actuator design and flight tests[25] were conducted. Data obtained from flight tests were found to compare favorably with prior CFD predictions and

demonstrated that controlled microflaps can generate reasonably high levels of lateral acceleration for projectile control.

Clearly, these new pin-based flow control mechanisms are unconventional, and more research is needed to fully understand the flow interaction effects and accurately predict the aerodynamics and flight performance. CFD offers a viable approach for obtaining aerodynamics of projectiles with traditional or unconventional flow control mechanisms. In 2024, Paul et al.[30,31] completed an investigation using an Euler code to evaluate the performance of different pin effector sizes in varied configurations for roll and pitch maneuvers and compared it with tail-flap control. Both Euler and Navier–Stokes techniques can be used in CFD simulations with pins. The Euler method solves the Euler equations (a simplified version of the Navier–Stokes equations), which are a set of quasilinear partial differential equations governing adiabatic inviscid flow. The Navier–Stokes equations are a set of partial differential equations that account for viscosity and hence include shock-/boundary-layer interactions. Thus, the Euler method produces very fast solutions compared with Navier–Stokes and is suitable for quick design studies involving pin control effectors; however, the viability of the Euler technique to accurately predict the aerodynamics for a projectile with multiple pin effectors has not yet been investigated.

The current investigation is a continuation of the 2024 research; it includes multiple pins for both pitch and roll control. The approach of this investigation is to compare pin effector aerodynamic performance calculated from both Euler and Navier–Stokes methods and also compare pin control performance with tail-flap control. This investigation seeks to determine the viability of using Euler methods to analyze projectiles with multiple pin effectors and also add more accurate viscous flow results to the aerodynamic database.

2. Geometry Definition

The baseline vehicle consisted of an axisymmetric ogive-cylinder body with four high-sweep, low-aspect ratio, clipped-delta fins. It featured a 3-cal. (1 cal. = 104.76 mm) long, blunt von Kármán ogive nose with a 0.1-cal. nose radius. The model had a slenderness ratio of 10. The root fin chord of the fins was 6 cal. long, the tip fin chord was 2.2 cal. long, and the fin span was 1.935 cal. Tail-flap control has been used to provide sufficient control authority to execute desired maneuvers.[32] The focus of this report is on the use of pin effectors to provide the control authority needed for control of the projectile. All simulations were performed with the tail-flap control undeflected, so the only control loads were due to the pin effectors.

Eight pin effector configurations were investigated over the course of this study. An example of a pin effector configuration is illustrated in Figure 1. The pin effectors are located 1.524 cal. from the base of the projectile. The pin effectors are simple rectangular prisms with an equal width and depth of 0.084 cal. (or 8.8 mm). Two pin height-to-width aspect ratios were used: 1.5 (primary) for a height of 0.126 cal. (13.2 mm) and 1 (short) for a height of 0.084 cal. (8.8 mm). All pin effectors are set 0.005 cal. above the projectile airframe for Euler simulations and intersecting the projectile airframe for Navier–Stokes simulations. The center of gravity (and moment reference point) was located 5.6 cal. from the nose for baseline and pin configurations.

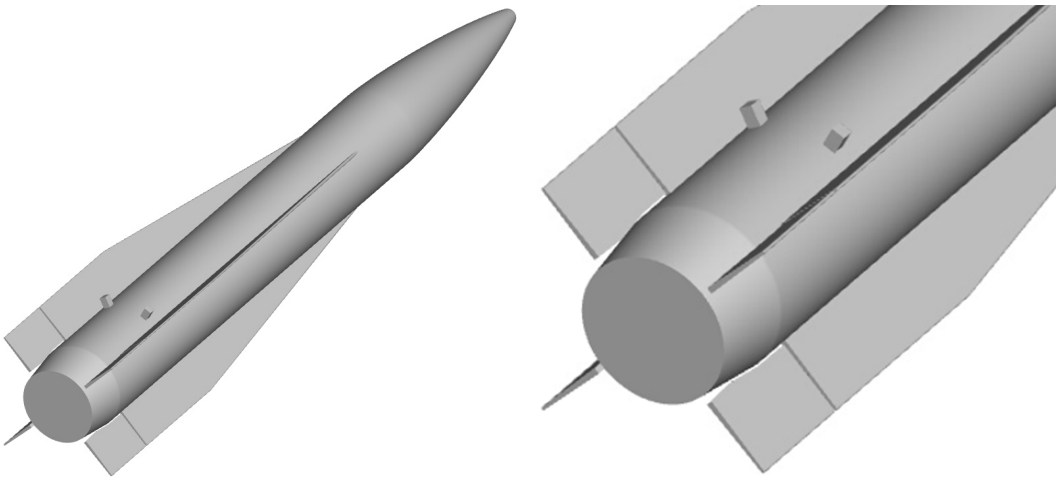

Figure 1. Flight vehicle with pin effectors symmetric on the lee side of the vehicle. The full projectile is shown on the left and a close-up view is shown on the right.

Five pin effector configurations were studied in this investigation to determine the control authority provided to a generic high-speed munition configuration for pitch control. The five variant configurations are made distinct by the presence of pin effectors as shown in Figure 2 (the baseline configuration is also shown for reference). The first variant configuration has one pin effector placed centered on the lee side of the airframe. The second configuration has two pin effectors set at 27° off vertical in both circumferential directions. The third variant configuration has two pin effectors set at 33° off vertical in both circumferential directions. The fourth configuration has three pin effectors with one pin effector in the center and two pin effectors set at 27° off vertical in both circumferential directions. Each of these variants had a height-to-width aspect ratio of 1.5. The fifth configuration is similar to the fourth, but with the shorter pins (height-to-width aspect ratio of 1.0).

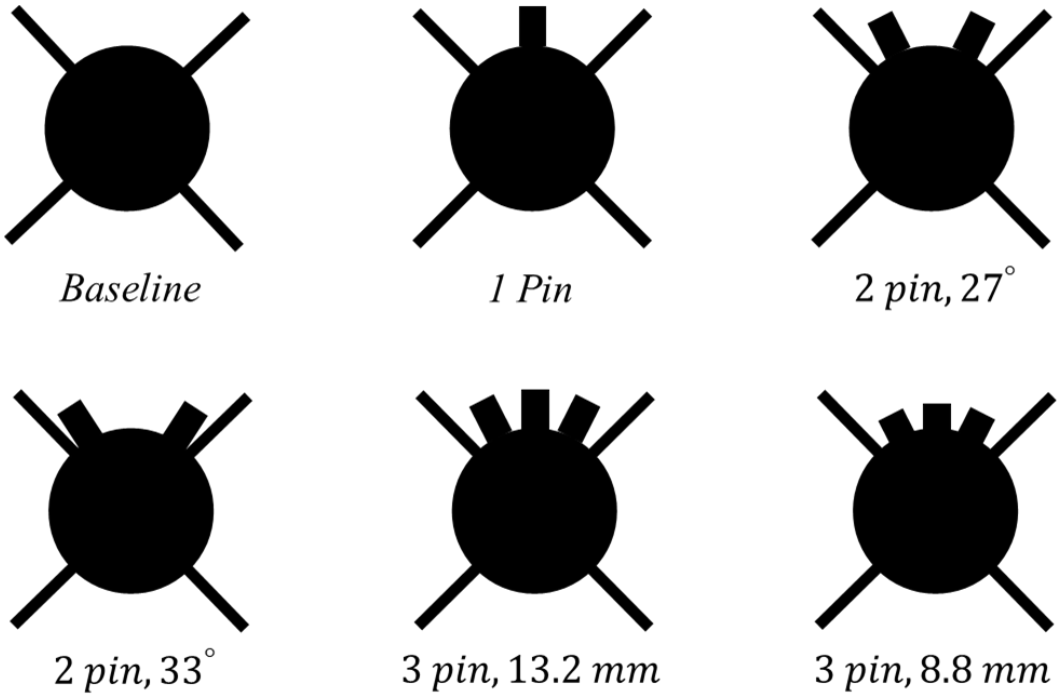

Figure 2. Conceptual diagrams (not to scale) of configurations analyzed.

For roll control, four configurations with pin effectors were considered in this study. In each configuration, four pins are used. Circumferentially, each pin is located close to a fin either at 27° or at 33° counterclockwise off the vertical axis or horizontal axis (Figure 3); the 33° orientation is much closer to the fin than the 27° case. Both pin heights were simulated in the Euler calculations, while only the 1.5 aspect ratio pin effectors were investigated in the Navier–Stokes simulations.

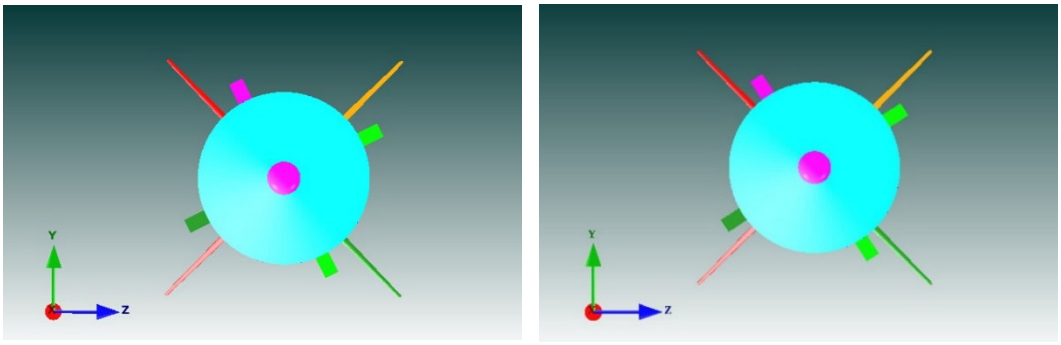

Figure 3. Computational model, y-z plane looking from the nose and showing the four-pin, 27° roll (left), and the four-pin, 33° (right) roll configurations, 0.126-cal. height.

3. Methodologies

Euler (inviscid) CFD and Reynolds-Averaged Navier–Stokes (RANS) CFD were used to generate aerodynamic coefficient data. Section 3.1 describes the implementation and execution of the Euler CFD software. Section 3.2 describes the implementation and execution of the RANS CFD software. All simulations were executed with the geometry oriented in the "x" configuration at a freestream Mach number of $M = 3$ and an angle of attack range of $-15° < \alpha < 15°$.

3.1 Euler CFD Software: Cart3D

The data was generated from simulations using a software package called Cart3D developed by NASA. NASA's Cart3D is an inviscid CFD package for quick aerodynamic design and analysis. Cart3D provides utility for surface modeling and intersection, mesh generation, flow simulation and postprocessing.[33] The mesh generation process automatically increases the fidelity of the domain near small features and curvature present in the geometry to better resolve flow features near the surface.

The meshes generated for the simulations consisted of approximately 11.56 million cells. This was the result of using 13 levels of refinement in a cartesian computational domain with an inscribed sphere of 7 body lengths. Perspectives of the meshes for the pitch configurations are shown in Figures 4–9; similar mesh refinement is used for the roll configurations. In Figures 5–9, the mesh plane in the left-hand image is located at 1.524 cal. from the base of the projectile or 2.876 cal. from the nose and 0.524 cal. from symmetry plane in the right-hand image. Aerodynamic coefficients for a given flight condition (i.e., Mach number and aerodynamic angles) are computed in several minutes by the flow solver, "flowCart." on Narwhal at the Department of Defense Supercomputing Resource Center.

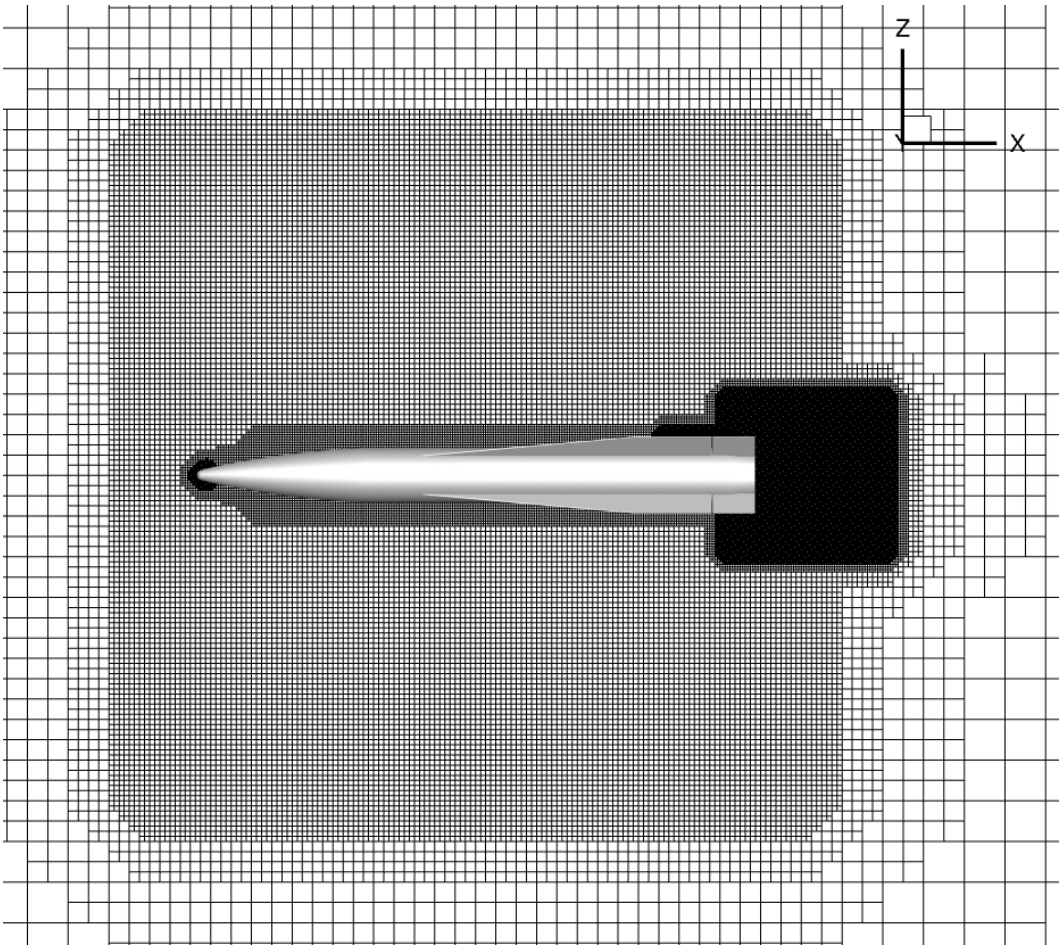

Figure 4. Example pitch plane mesh view.

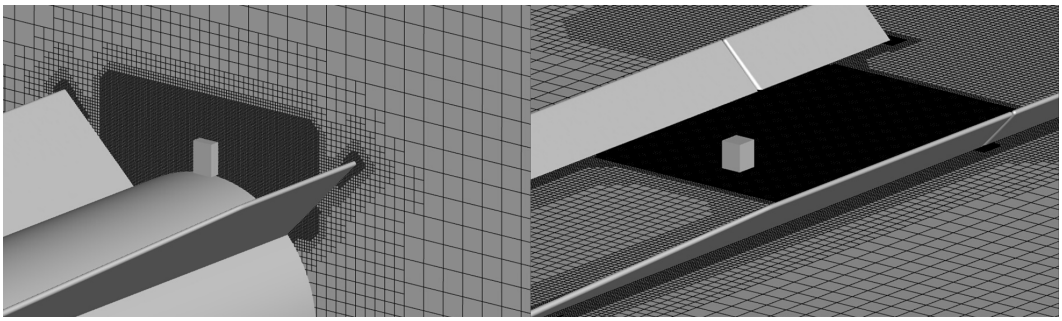

Figure 5. Detailed views of the mesh in the region of the pin effector of the one-pin configuration.

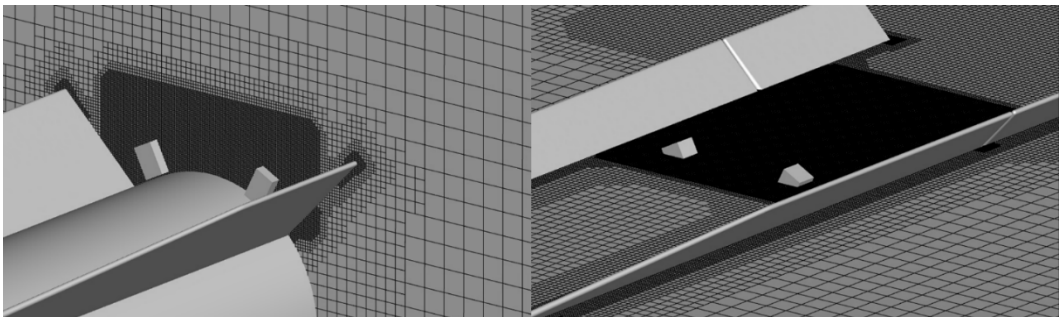

Figure 6. Detailed views of the mesh in the region of the pin effector of the two-pin, 27° configuration.

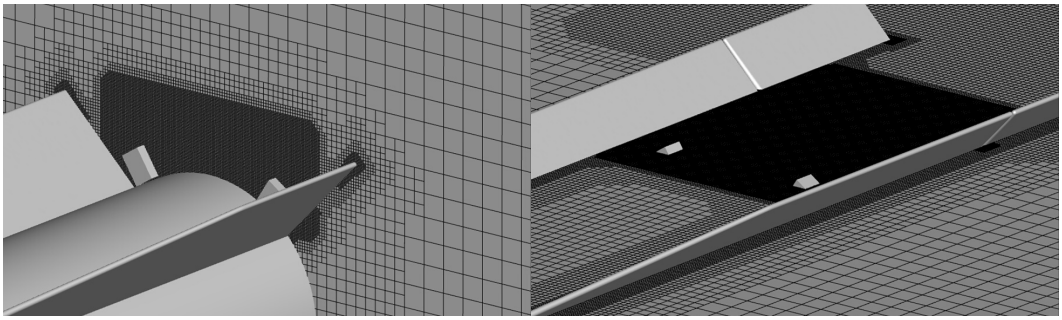

Figure 7. Detailed views of the mesh in the region of the pin effector of the two-pin, 33° configuration.

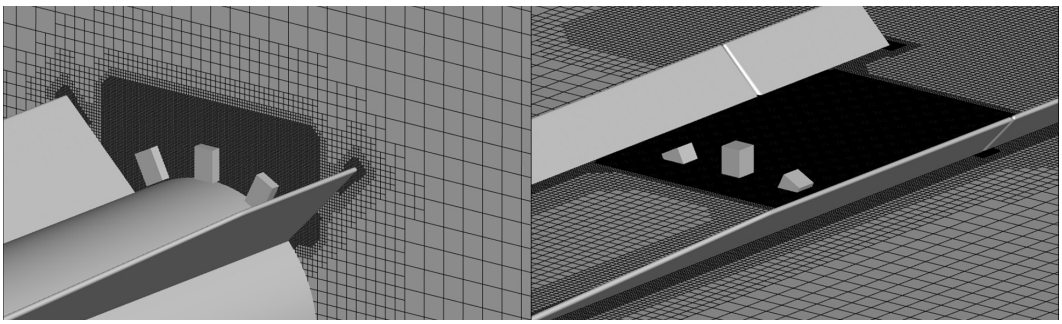

Figure 8. Detailed views of the mesh in the region of the pin effector of the three-pin, 13.2-mm configuration.

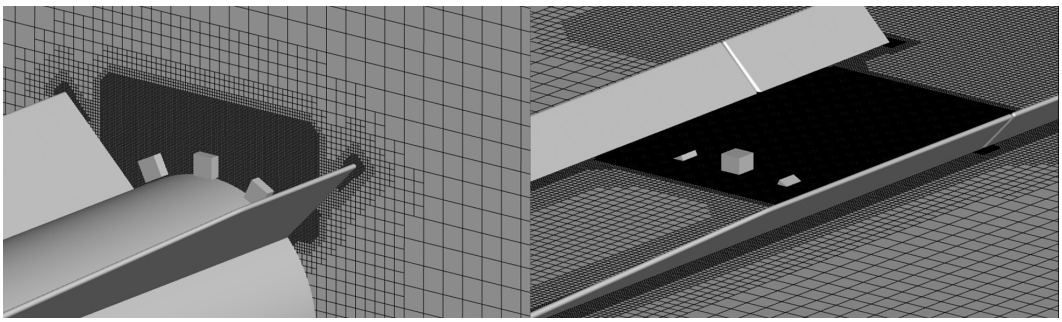

Figure 9. Detailed views of the mesh in the region of the pin effector of the three-pin, 8.8-mm configuration.

3.2 Navier–Stokes CFD code: CFD^{++}

The complete set of 3-D time-dependent Navier–Stokes equations is solved in a time-asymptote manner to obtain converged steady-state solutions. A commercially available code, CFD++,[34,35] is used; and the 3-D, time-dependent RANS equations are solved using the following finite volume method:

$$\frac{\partial}{\partial t}\int_V \mathbf{W}dV + \oint [\mathbf{F} - \mathbf{G}] \cdot dA = \int_V \mathbf{H}dV \tag{1}$$

where **W** is the vector of conservative variables, **F** and **G** are the inviscid and viscous flux vectors, respectively, **H** is the vector of source terms, V is the cell volume, and A is the surface area of the cell face.

Several techniques, such as implicit scheme and relaxation, are used to achieve faster convergence. Use of an implicit scheme circumvents the stringent stability limits suffered by their explicit counterparts, and successive relaxation allows update of cells as information becomes available and thus aids convergence. Second-order discretization was used for the flow variables and the turbulent viscosity equation. The turbulence closure is based on topology-parameter-free formulations. A realizable two-equation k-ϵ turbulence model[36] was used for the computation of turbulent flows. These models are ideally suited to unstructured bookkeeping and massively parallel processing due to their independence from constraints related to the placement of boundaries and/or zonal interfaces. The basic CFD solution technique described here was used to obtain steady-state solutions using the time-marching implicit scheme. Converged solutions were obtained with an approximately 6 orders of magnitude drop in the residuals. The computational model for the RANS CFD simulations is shown in Figure 10. It clearly shows each of the body components (i.e., nose, front body, main body, rear body, front fins, rear fins, pins) as modeled in the RANS simulations.

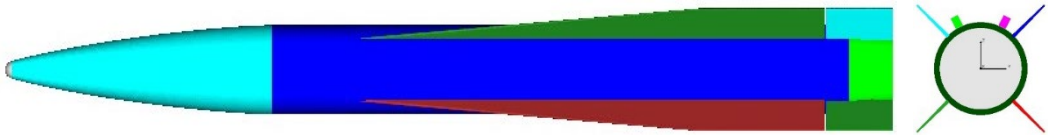

Figure 10. Computational model, x-z plane (left) and y-z plane (right) showing the two-pin, 27° configuration.

The computational mesh used was generated using multipurpose intelligent meshing environment (MIME),[37] an unstructured mesh generator developed by Metacomp Technologies, Inc. The total mesh size was approximately 76 million cells, consisting of triangular surface cells, with prism layers used along the surface

and tetrahedral cells for the rest of the domain. The computational domain extended approximately 20 projectile calibers in all directions from the center of the projectile. The average cell size of the cylindrical density box (i.e., 2 cal. in radius, spanning 1 cal. forward to 5 cal. back of the projectile) was approximately 0.019 cal. The first cell wall spacing of the prism layers was set to 3×10^{-6} cal. to ensure y+ values of less than or equal to 1 along the surface of the projectile. The boundary-layer spacing near the wall was selected so that a wall boundary condition that integrates all the way to the wall could be used for turbulent flow calculations.

A close-up view of the computational mesh near the body used for numerical Navier–Stokes simulations is presented in Figure 11. Figure 12 shows a cross-sectional view of the body or background mesh at a location just past the pins. An unstructured mesh was first obtained for the projectile without the movable flaps and pins. Unstructured meshes were then generated about each rear fin flap and pin effector separately. The flap and pin effector meshes are then overset with the background projectile mesh to obtain a Chimera overlapped mesh for the finned projectile with fin flaps and pins. The advantage is that the individual flap and pin effector meshes were generated once, and the Chimera procedure can then be applied repeatedly as required during the flap or pin effector motion without the need to generate the meshes at each time for the simulations. Specifically for the pins, the full pin effector meshes each with about 200,000 cells are shown in Figure 13. The outer boundary of the pin effector meshes gets information from the background body mesh. The pin effector and the body cut holes into each other's mesh; an example of the pin effector cutting a hole into the body mesh is shown on the right in Figure 13.

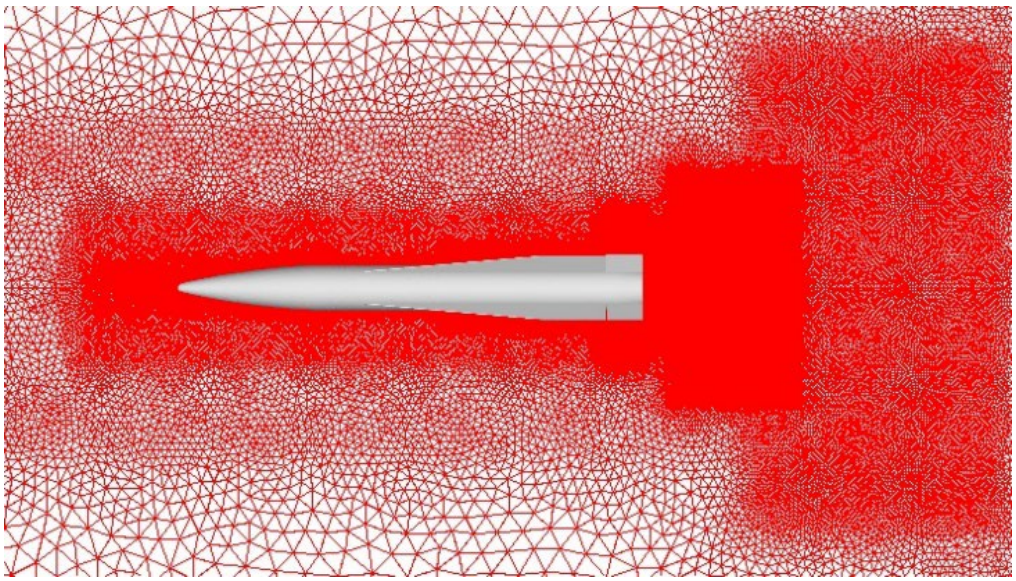

Figure 11. Computational mesh expanded near the body.

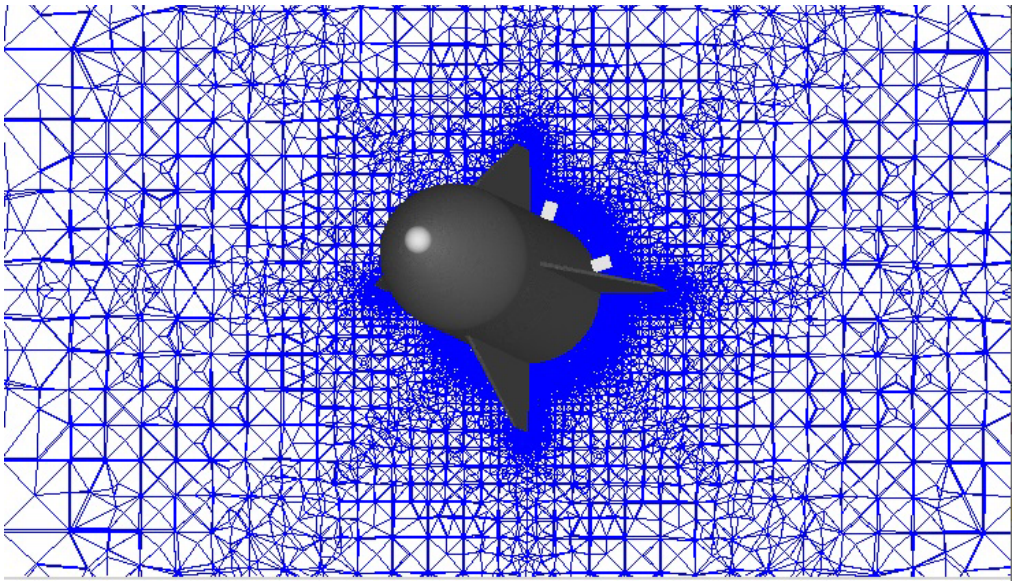

Figure 12. Computational mesh at a cross section through the fins (past the pins).

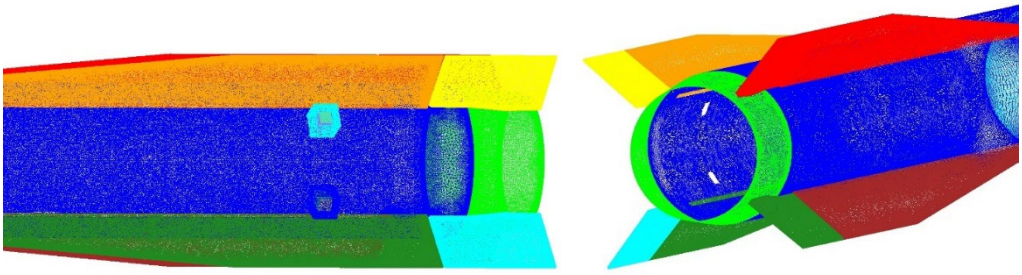

Figure 13. Computational body surface mesh and pin effector meshes (left) with holes cut by the pin effector on the body (right).

4. Results

Steady-state CFD computations were performed using Euler (Cart3D) and RANS technique (CFD++) for both pitch and roll control. All simulations were run at a freestream Mach number of $M = 3$ and angles of attack range of $-15° < \alpha < 15°$. The results of this investigation are separated into two subsections. Section 4.1 presents computational results obtained for pitch control. The roll control results are presented in Section 4.2.

4.1 Pitch Control Simulations

In the pitch control investigation six configurations were simulated and analyzed. Five configurations have pin effectors. The baseline configuration (no pin effectors) was also studied in this investigation for comparison purposes. Subsection 4.1.1 presents multiple perspectives showing pressure distribution over the projectile, and computed flow field around the projectile and within the

immediate proximity of the pin effector. Subsection 4.1.2 presents the results for pin effector aerodynamic performance obtained from both the Euler simulations and the RANS simulations.

4.1.1 Flow-Field Analysis

The Mach and C_p contours for the one-pin, two-pin, 27°, and three-pin, 13.2-mm configurations were calculated using the Euler code and are shown in Figures 14–16. Analyzing the surface pressure (C_p contour) calculated for $\alpha = -15°$ in the top right of Figure 14, there is a high-pressure region that develops in front of the pin effector and there is a recompression region behind the pin effector. The high-pressure regions created by the pin effectors behind the center of pressure generate a negative C_N ($-z$ direction) contribution and a positive C_m (nose-up) contribution.

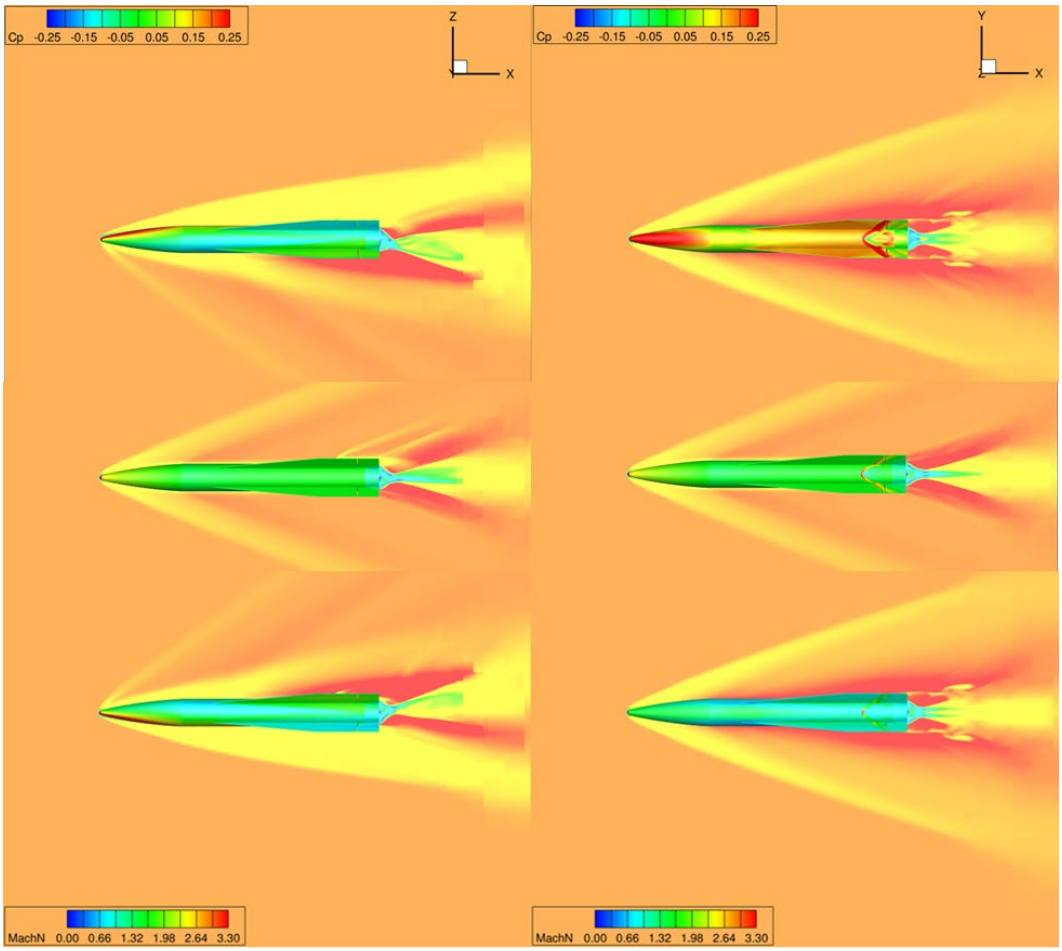

Figure 14. Mach and C_p contours of the Euler simulations for the one-pin configuration as viewed from the side (left) and the top (right) at $\alpha = -15°$ (top), $\alpha = 0°$ (middle), and $\alpha = 15°$ (bottom).

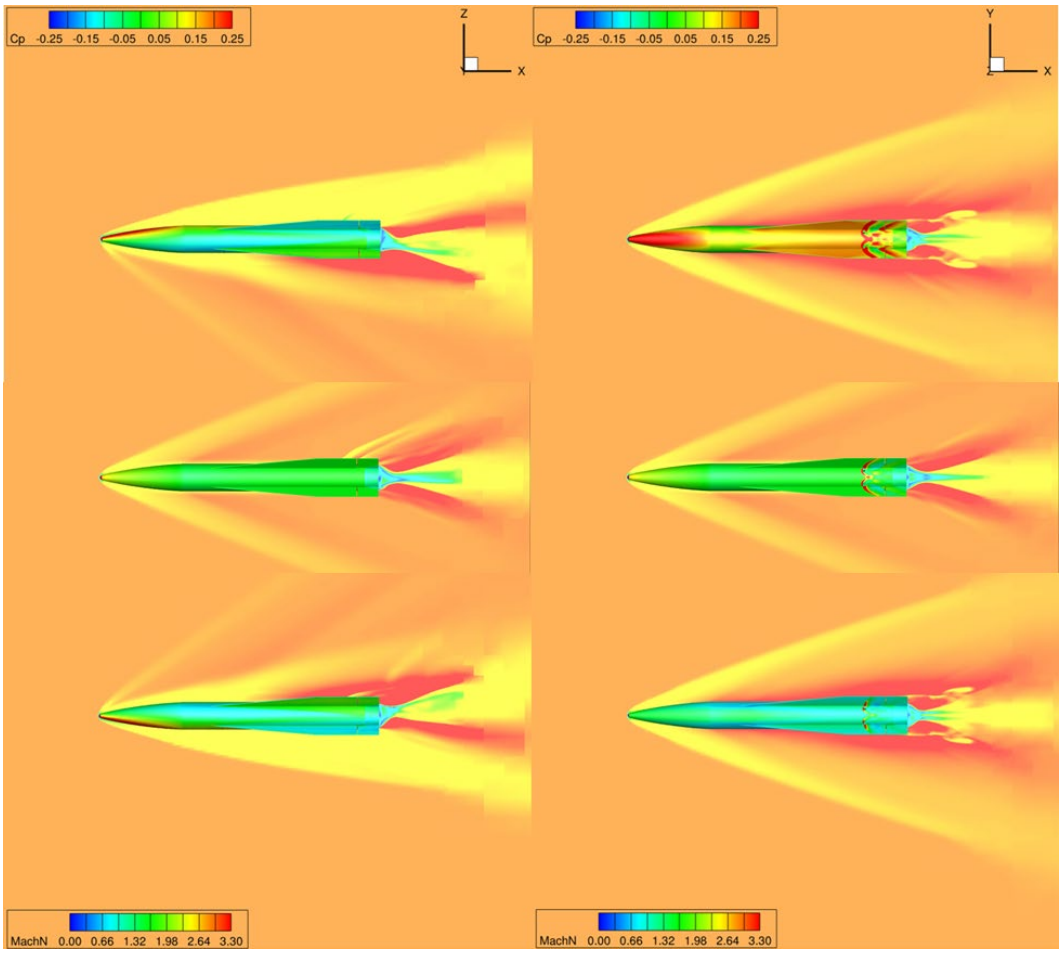

Figure 15. Mach and C_p contours of the Euler simulations for the two-pin, 27° configuration as viewed from the side (left) and the top (right) at α = –15° (top), α = 0° (middle), and α = 15° (bottom).

The high-pressure regions created by the pin effector(s) is larger, and should be more effective, as α becomes more negative as the pins are on the wind side of the body. Conversely, the high-pressure region created by the pin effector(s) is smaller (and less effective), as α becomes more positive as the pins are on the lee side of the body. As shown later, the pins still provide some control authority when in the shadow of the body, even at the highest incidence angles. This concept is illustrated by contrasting the top right C_p contour with the bottom right C_p contour in Figure 14. Analyzing the C_p contours calculated for the two-pin, 27°, and the three-pin, 13.2-mm configurations at α = –15° in the top right of Figures 15 and 16, there are high-pressure regions that develop in front of the pin effectors as well as recompression regions behind the pin effectors similar to the one-pin configuration. Another similarity to the one-pin configuration is the significant decrease in the high-pressure regions both in front of and behind the pin effectors at positive α. Focusing on the Mach and C_p contours of the one-pin, two-pin, 27°, and three-pin, 13.2-mm configurations, as viewed from the side at nonzero α in Figures 14–16,

the asymmetric wake includes the impact of the flow field around the pin effectors. This impact is easier to observe at positive α since the lower Mach number in the vicinity of the pin effectors contrasts with the higher Mach number as the lee-side flow expands around the body of the projectile.

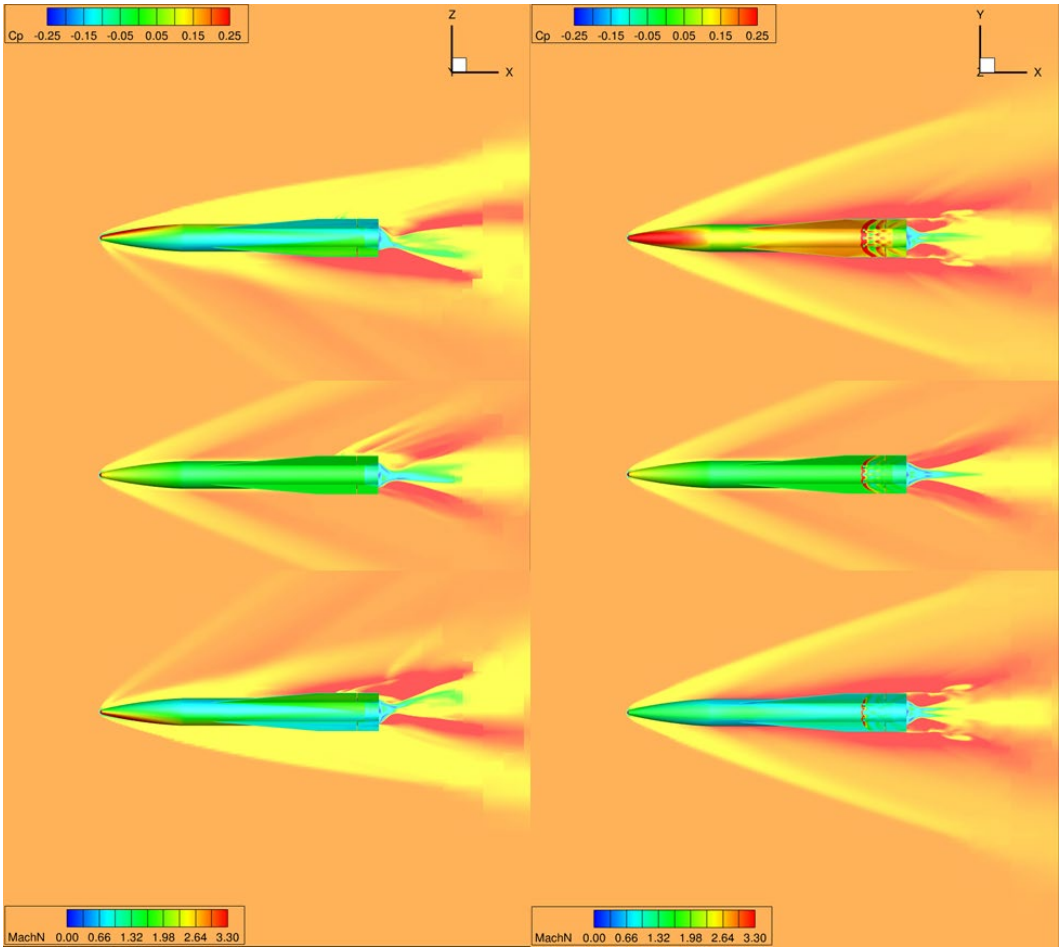

Figure 16. Mach and C_p contours of the Euler simulations for the three-pin, 13.2-mm configuration as viewed from the side (left) and the top (right) at $\alpha = -15°$ (top), $\alpha = 0°$ (middle), and $\alpha = 15°$ (bottom).

The cause of negative C_N contribution and a positive C_m contribution produced by the pin effectors (as will be seen in Section 4.1.2) is isolated by focusing on the differences in surface pressure distribution immediately surrounding the pin effectors on both the lee side and wind side of the projectile for the two-pin, 27° configuration at $\alpha = 0°$ (Figure 17). The asymmetry in pressure distribution between the lee side and the wind side even at $\alpha = 0°$ is readily apparent.

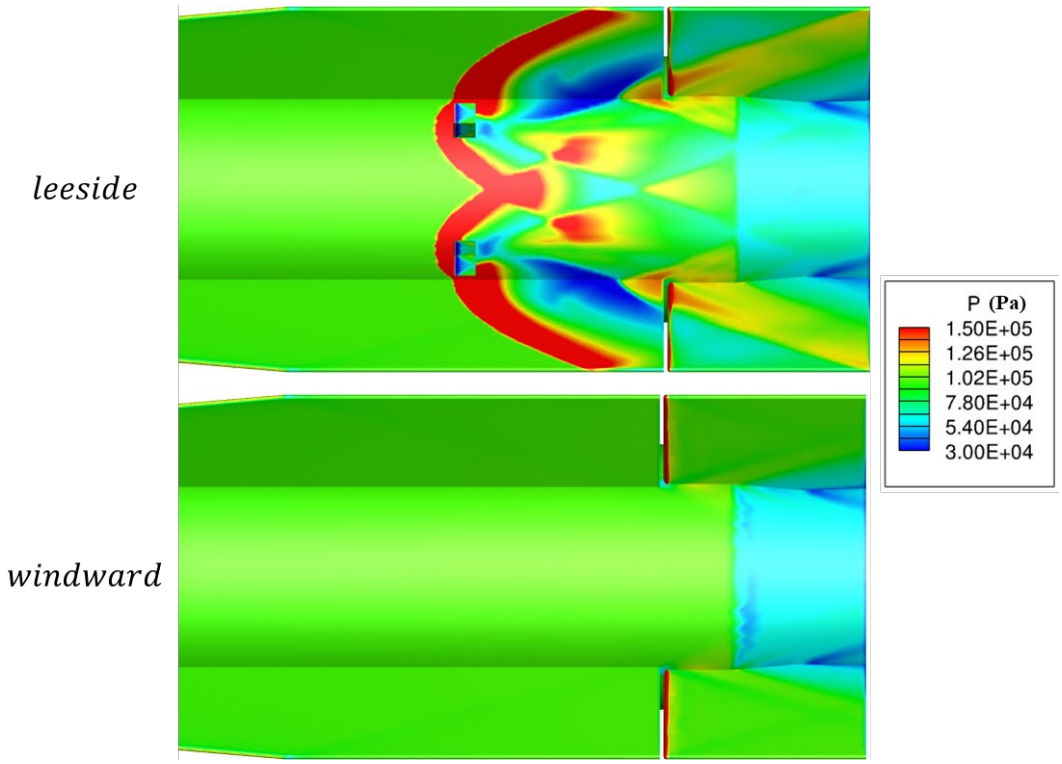

Figure 17. Lee side and wind side Euler surface pressure of the two-pin, 27° configuration at α = 0°.

The pin effector pressure phenomenon is illustrated in greater detail for the one-pin, two-pin, 27°, and three-pin, 13.2-mm configurations in Figures 18 and 19 (note the different pressure scale in each figure). A qualitative observation can be made about Figure 16 ($\alpha \geq 0°$) that the pin effectors are able to generate high-pressure regions at all angles of attack that are likely sufficient to offset small regions of low pressures behind the pins and thus maintain reasonable effectiveness at high angles of attack, such as $\alpha \geq 10°$ and possibly at $\alpha = 15°$. This is an interesting observation because it would have been intuitive to expect the pin effectors become less effective on the lee side of the vehicle in the shadow of the forebody. This observation will be quantified in Section 4.1.2. The surface pressure contours at various α in Figures 18 and 19 show how the high-pressure regions both in front of and behind the pin effectors decrease in size and intensity as α increases. This trend is evident in both RANS and Euler surface pressure contours.

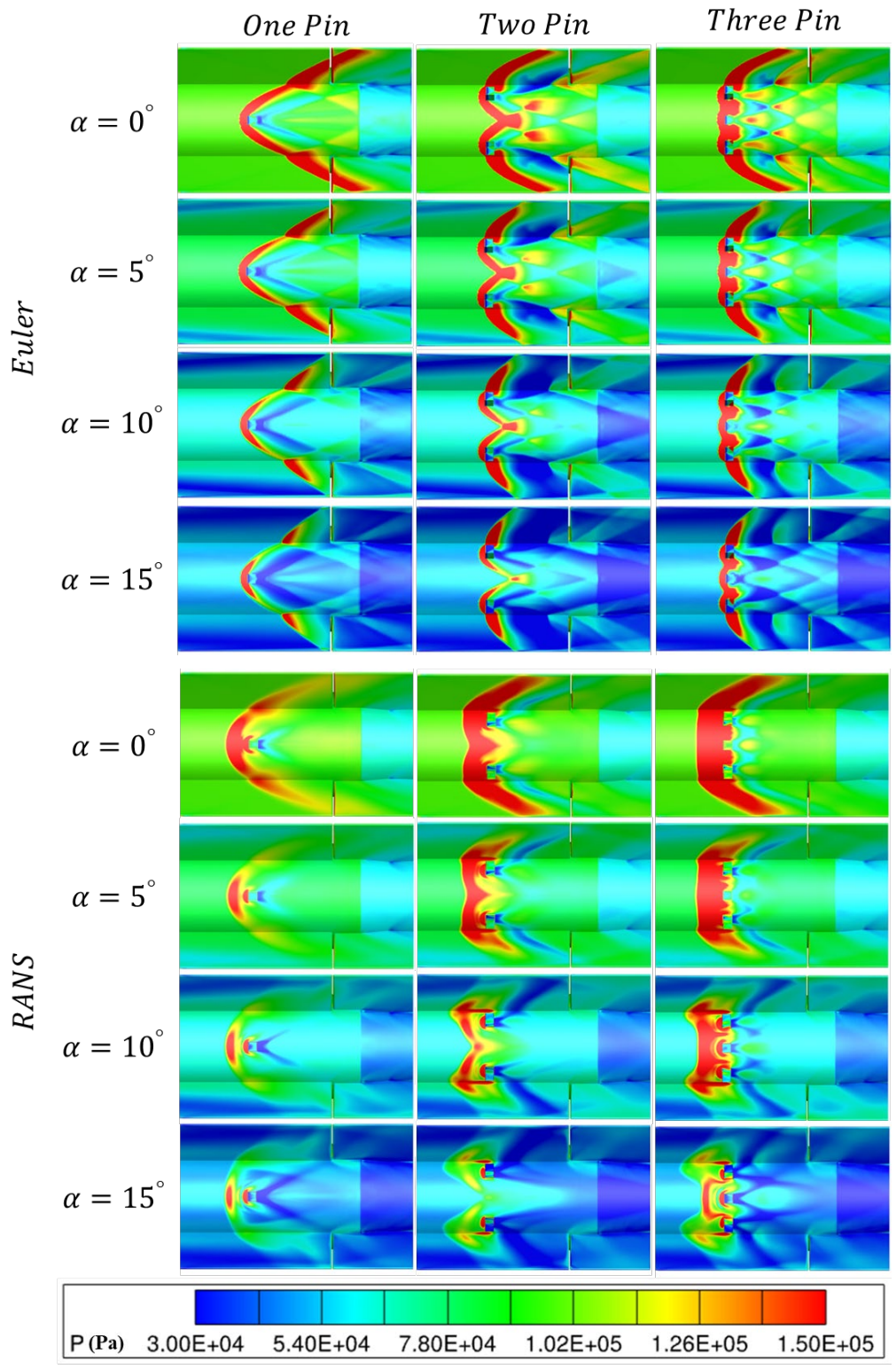

Figure 18. Surface pressure contours showing detail near the pin effectors for Euler simulations (top four rows) and RANS simulations (bottom four rows) comparing the one-pin, two-pin, 27°, and three-pin, 13.2-mm configurations at selected positive α from α = 0° to α = 15°.

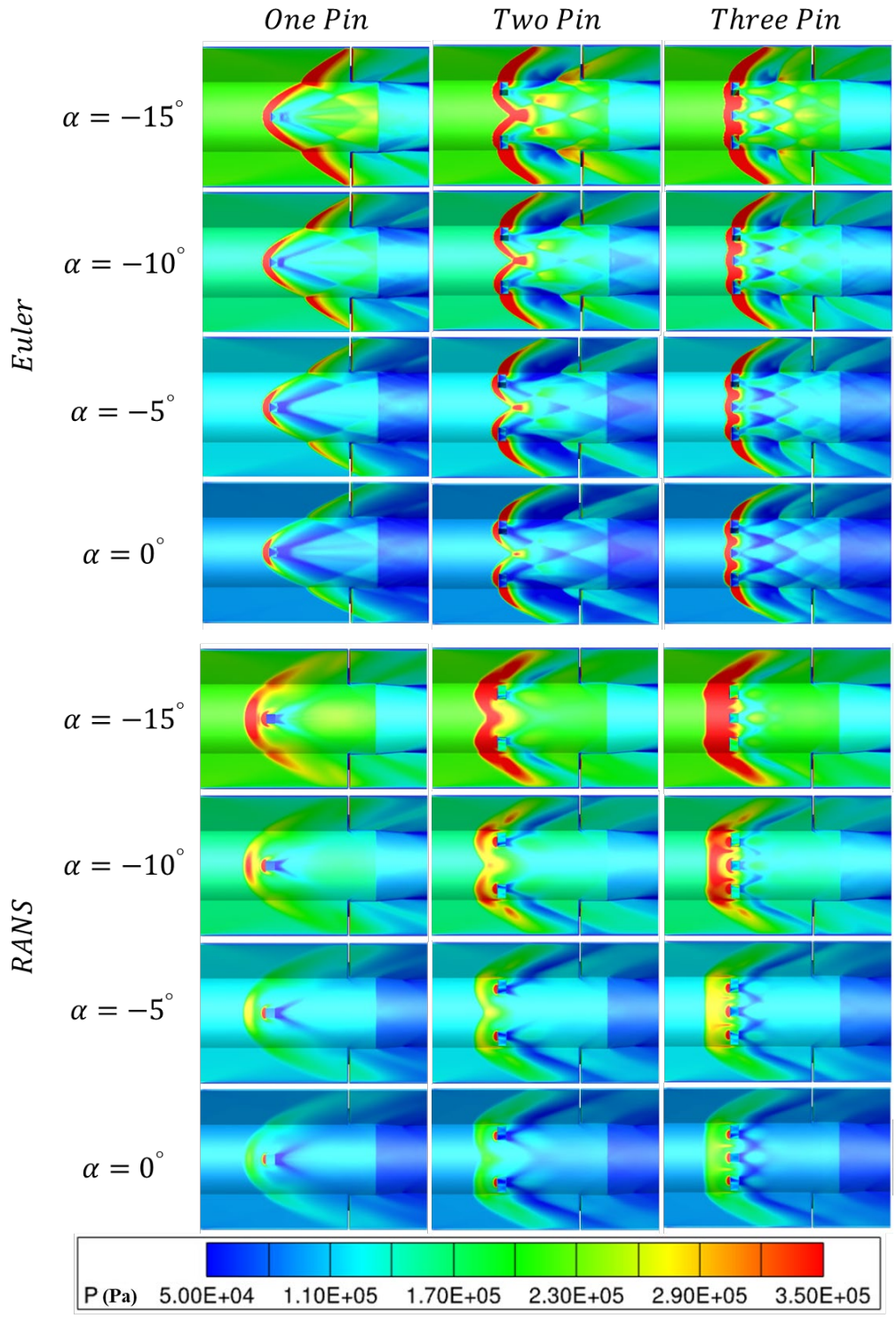

Figure 19. Surface pressure contours showing detail near the pin effectors for Euler simulations (top four rows) and RANS simulations (bottom four rows) comparing the one-pin, two-pin, 27°, and three-pin, 13.2-mm configurations at selected negative α from α = –15° to α = 0°.

However, there are some important differences comparing the RANS and Euler surface pressure contours. There is greater curvature in the intersecting shock structure in the Euler contours compared with the RANS contours. The shock intersection is sharper in the Euler contours (no shock-boundary layer interactions), while the shock intersection forms a more connected region in the RANS contours. There is also a greater shock stand-off distance in the RANS contours compared with the Euler contours. The flow structures behind the pin effectors are significantly less pronounced in the RANS contours compared with the Euler contours.

Comparing the configurations of different pin effector quantities in Figures 18 and 19, the Euler simulations show a similar shock structure for each pin effector quantity across all α. This is also true for the RANS simulations for the one-pin configuration but not for the two-pin, 27°, and three-pin, 13.2-mm configurations. The RANS simulations for the two-pin, 27°, and three-pin, 13.2-mm configurations show the similar shock structure for all negative α and low-positive α, but the shock structure starts to change noticeably between α = 5° and α = 10°. The shock–shock interactions are weaker at α = 10° and are much weaker at α = 15°

Comparing the RANS simulations for the two, 2-pin configurations (Figures 20 and 21), there are subtle differences. The shock–shock interaction is more prominent in the body region in between the two pins for the 2-pin, 27° configuration compared with the 2-pin, 33° configuration. Additionally, the low-pressure regions behind the pin effectors are more evident for the two-pin, 33° configuration compared with the two-pin, 27° configuration. However, for the most part, the differences between the two, 2-pin configurations are small. The consequences (or lack of consequences) from these differences are discussed in detail in Section 4.1.2 on aerodynamic performance.

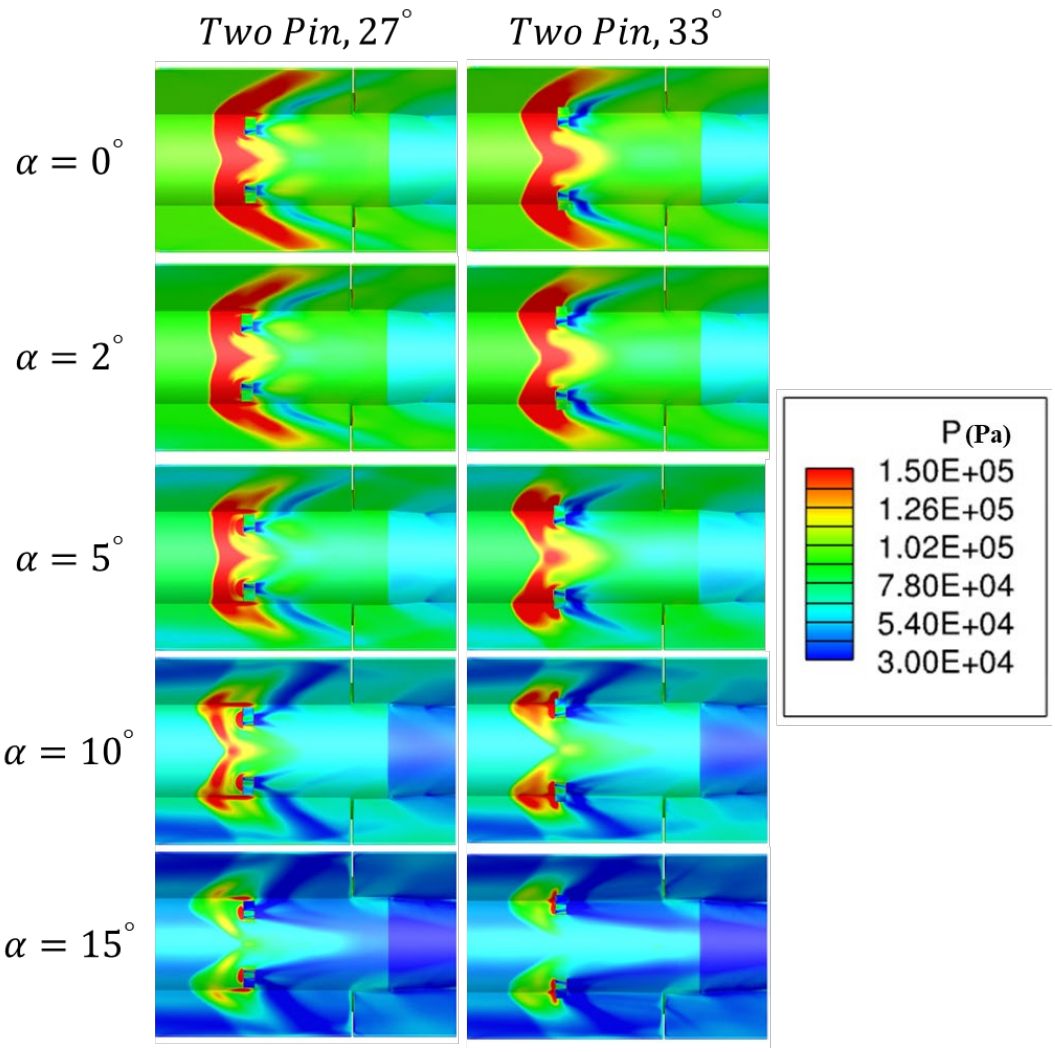

Figure 20. Surface pressure contours showing detail near the pin effectors for RANS simulations comparing the two-pin, 27°, and two-pin, 33° configurations at selected positive α from $\alpha = 0°$ to $\alpha = 15°$.

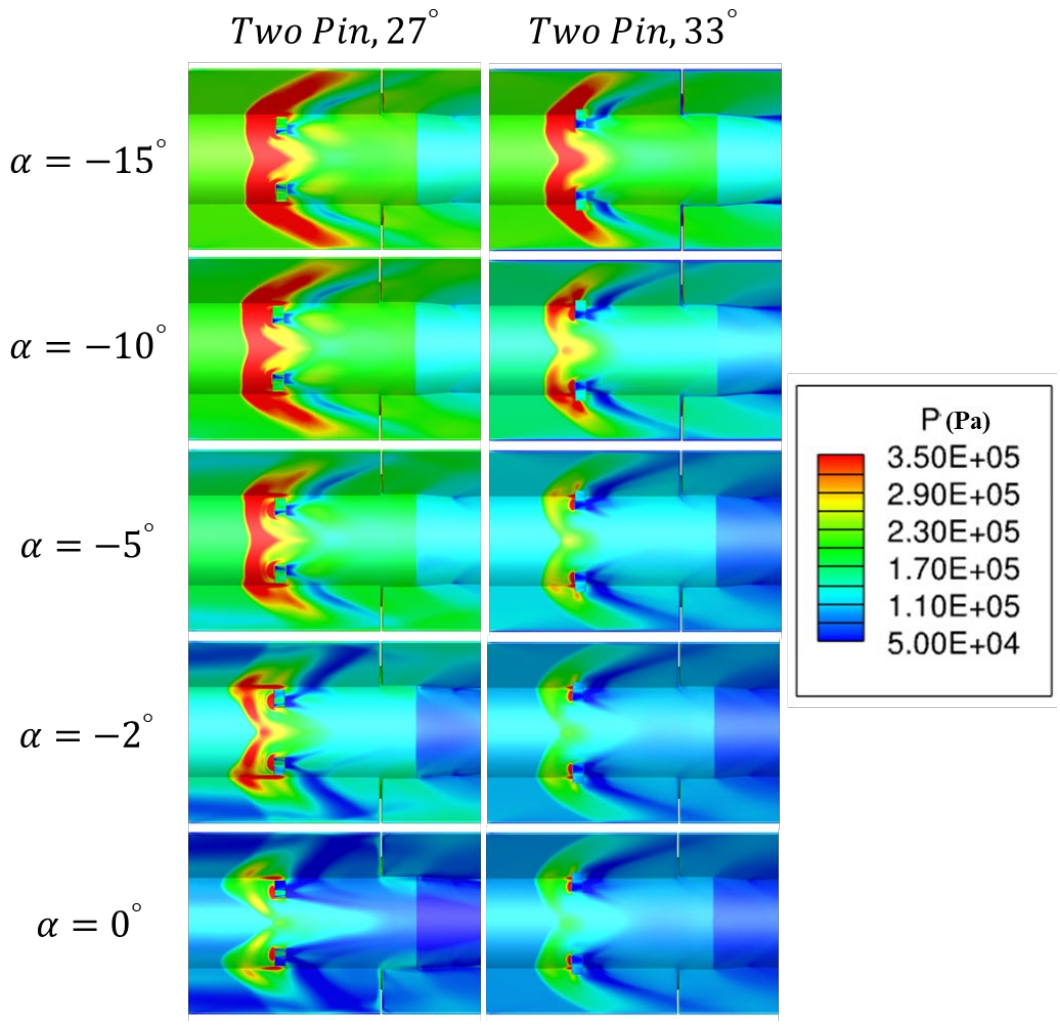

Figure 21. Surface pressure contours showing detail near the pin effectors for RANS simulations comparing the two-pin, 27°, and two-pin, 33° configurations at selected negative α from $\alpha = -15°$ to $\alpha = 0°$.

Similar to comparing the RANS simulations for the two 2 pin configurations, the comparison of the two 3-pin configurations (Figures 22 and 23) also shows some differences. As expected, the shock stand-off distance (as indicated by the end of the high-pressure region) for the taller three-pin, 13.2-mm configuration is greater than the shock stand-off distance for the shorter three-pin, 8.8-mm configuration. As with the 2-pin configurations, there are not dramatic differences between the two 3-pin configurations.

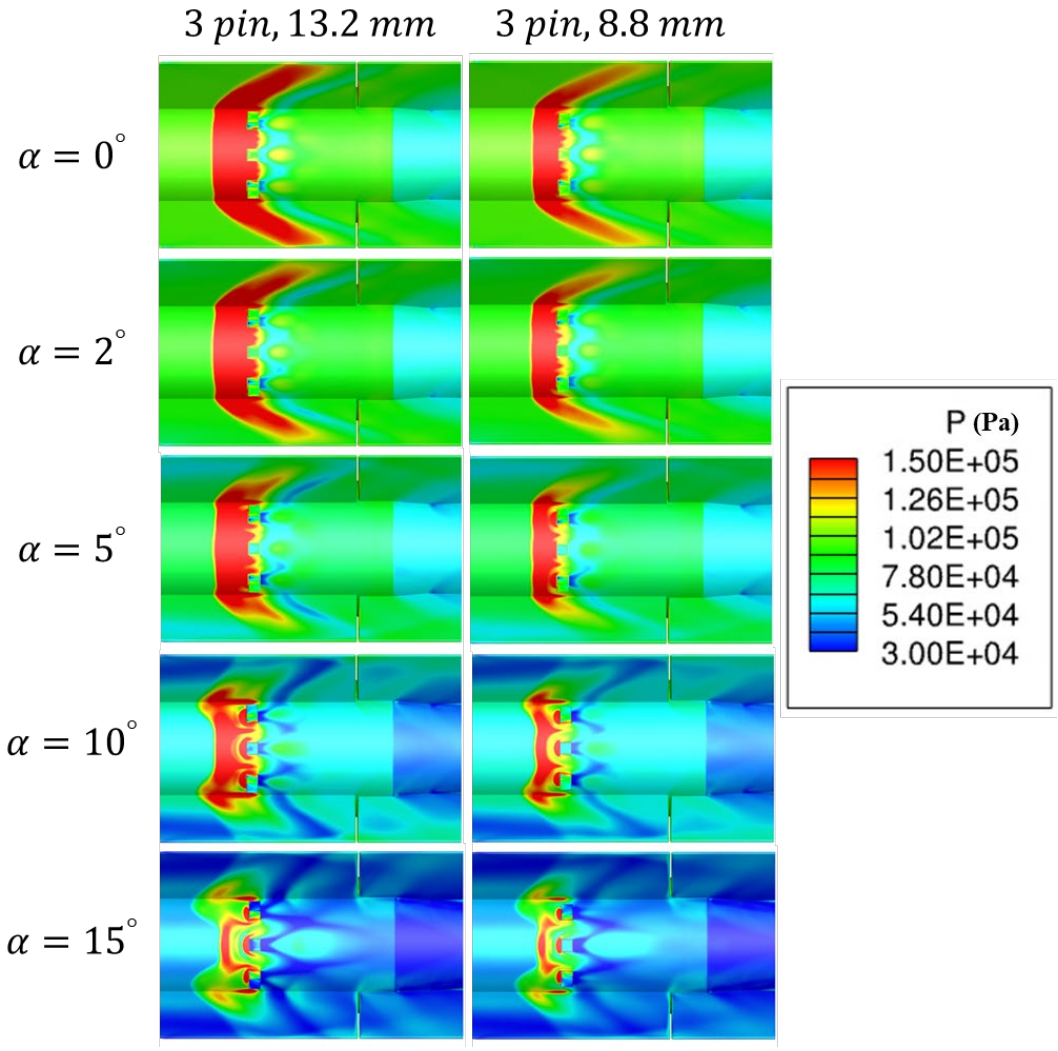

Figure 22. Surface pressure contours showing detail near the pin effectors for RANS simulations comparing the three-pin, 13.2-mm, and three-pin, 8.8-mm configurations at selected positive α from $\alpha = 0°$ to $\alpha = 15°$.

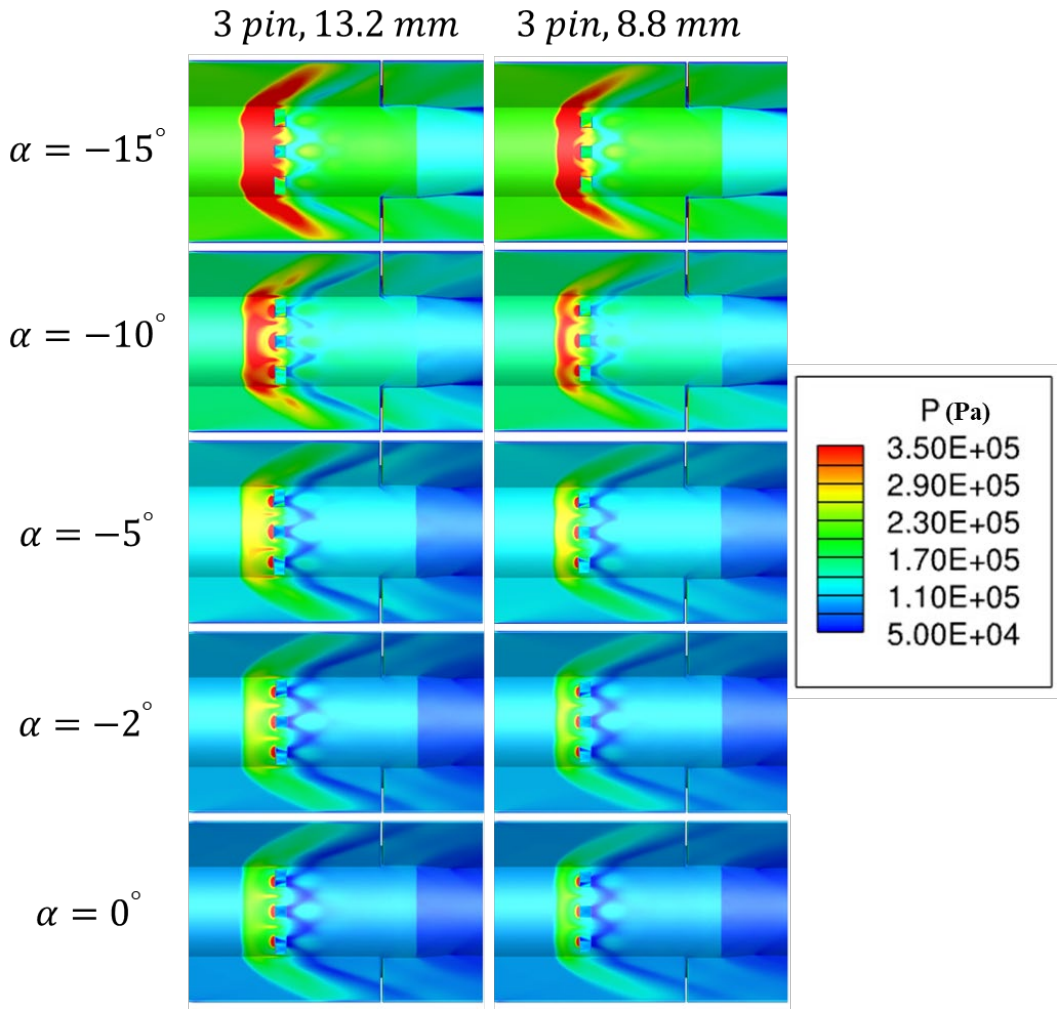

Figure 23. Surface pressure contours showing detail near the pin effectors for RANS simulations comparing the three-pin, 13.2-mm, and three-pin, 8.8-mm configurations at selected negative α from $\alpha = -15°$ to $\alpha = 0°$.

Qualitatively, differences are observed between the results of the Euler and RANS simulations. These differences are attributed to the inclusion of viscosity in the Navier–Stokes equations. While Euler simulations can account for inviscid shock–shock interactions, the inclusion of viscosity enables RANS simulations to account for more complicated phenomenon, such as shock-boundary layer interaction and the impact of body vortex roll-up from the air frame of the projectile. For instance, the surface pressure contours at $\alpha = 15°$ show the RANS simulations capturing the separation of the high-pressure region in front of the pin effectors (see Figure 18, bottom).

4.1.2 Aerodynamic Performance

The primary aerodynamic metrics that this investigation is concerned with are C_N, C_m, and C_A. The raw data and coefficient increment, ΔC, plots for C_N are displayed in Figures 24 and 25, for C_m in Figures 26 and 27, and for C_A in Figures 28 and 29. The coefficient increment values were calculated by subtracting the baseline aerodynamic coefficients from the variant configuration aerodynamic coefficients with pin effectors (Equations 2–4).

$$\Delta C_N = C_{N_{pin}} - C_{N_{baseline}} \tag{2}$$

$$\Delta C_m = C_{m_{pin}} - C_{m_{baseline}} \tag{3}$$

$$\Delta C_A = C_{A_{pin}} - C_{A_{baseline}} \tag{4}$$

Analyzing the C_N plots in Figure 24, there appears to be relatively little difference among the values generated by either Euler or RANS simulations for all three configurations. However, analyzing the ΔC_N plots in Figure 25, differences are observable. Yet, it is also important to note that the range of the ΔC_N plots is significantly smaller than that of the C_N plots. Focusing on the one-pin, two-pin, 27°, and three-pin, 13.2-mm configurations (left plot in Figure 25), ΔC_N increases with increasing number of pins, as would be expected. Also, the Euler data overpredicts the magnitude of the ΔC_N contribution from the pin effectors for all α compared with the RANS data. This overprediction is exacerbated at negative α. The overprediction also increases with increasing the number of pins, indicating that the Euler code is likely not correctly predicting the shock interactions among the pins.

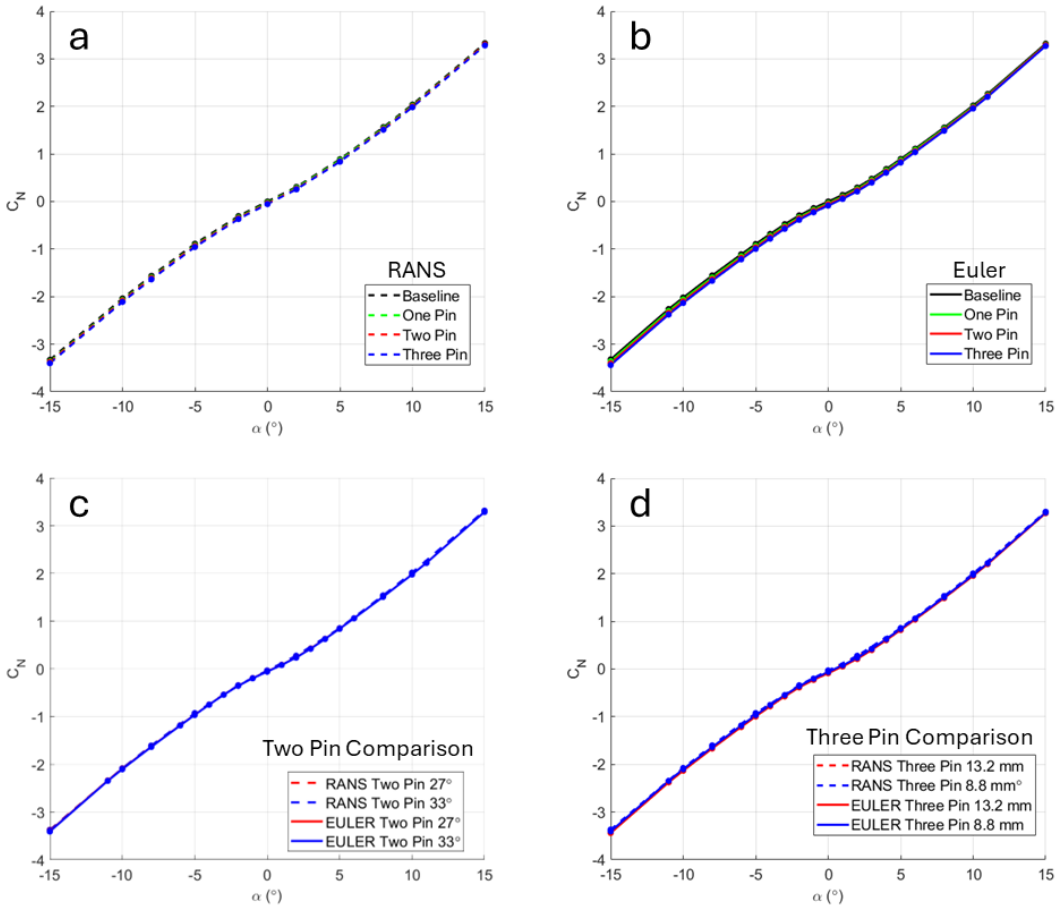

Figure 24. C_N **calculated from RANS (a) and Euler (b) simulations for the one-pin, two-pin, 27°, and three-pin, 13.2-mm configurations; and for the two-pin (c) and three-pin configurations (d).**

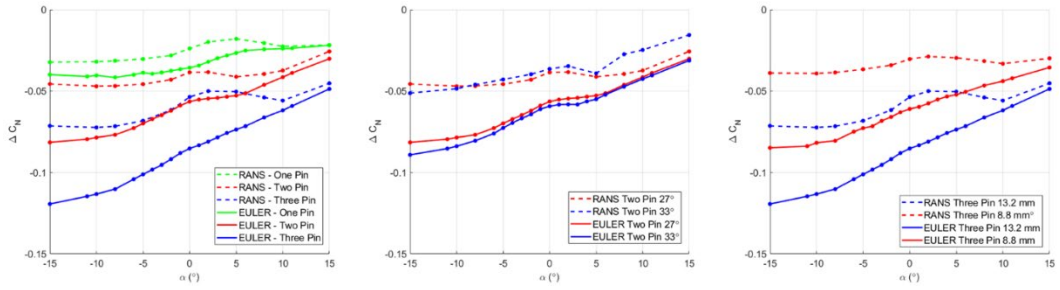

Figure 25. ΔC_N **calculated from RANS and Euler simulations for the one-pin, two-pin, 27°, and three-pin, 13.2-mm configurations (left), the two, 2-pin configurations (middle) and the two, 3-pin configurations (right).**

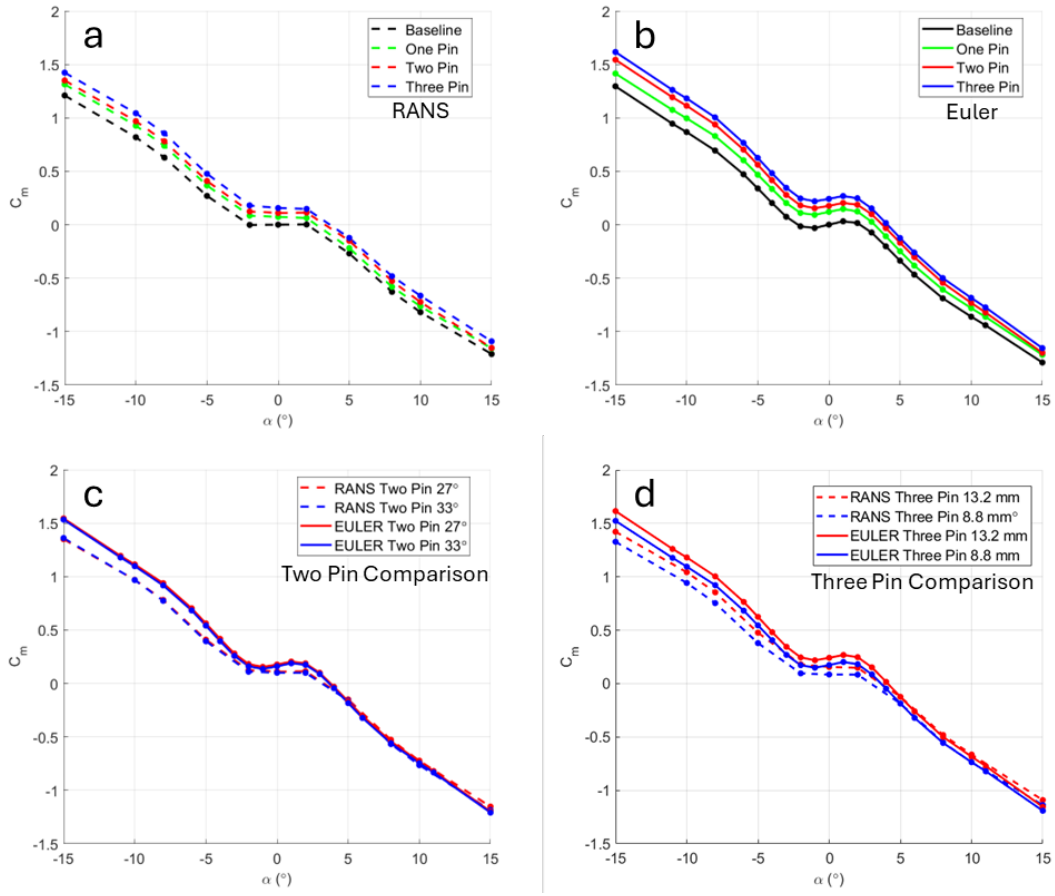

Figure 26. C_m **calculated from RANS (a) and Euler (b) simulations for the one-pin, two-pin, 27°, and three-pin, 13.2-mm configurations; and for the two-pin (c) and three-pin configurations (d).**

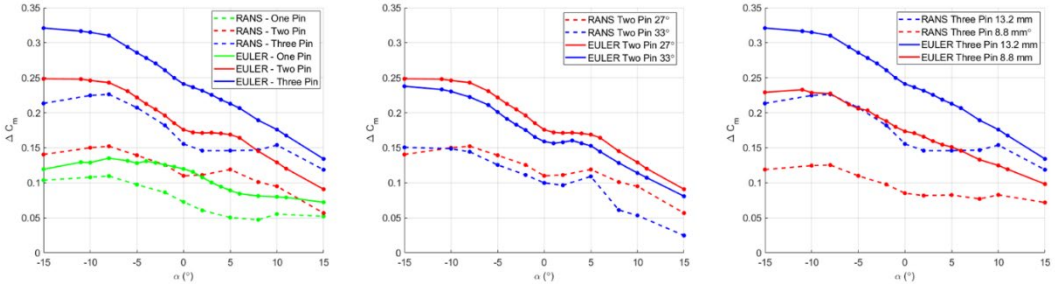

Figure 27. ΔC_m **calculated from RANS and Euler simulations for the one-pin, two-pin, 27°, and three-pin, 13.2-mm configurations (left); the two, 2-pin configurations (middle); and the two, 3-pin configurations (right).**

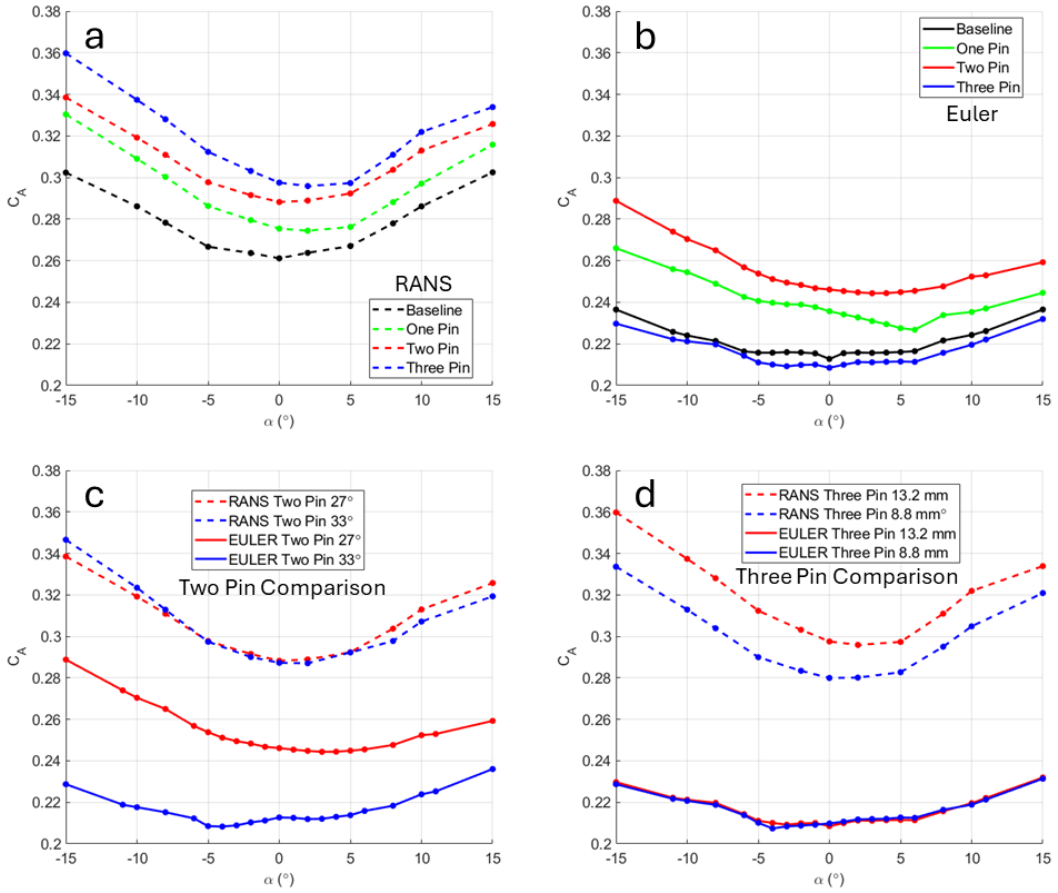

Figure 28. C_A **calculated from RANS (a) and Euler (b) simulations for the one-pin, two-pin, 27°, and three-pin, 13.2-mm configurations; and for the two-pin (c) and three-pin configurations (d).**

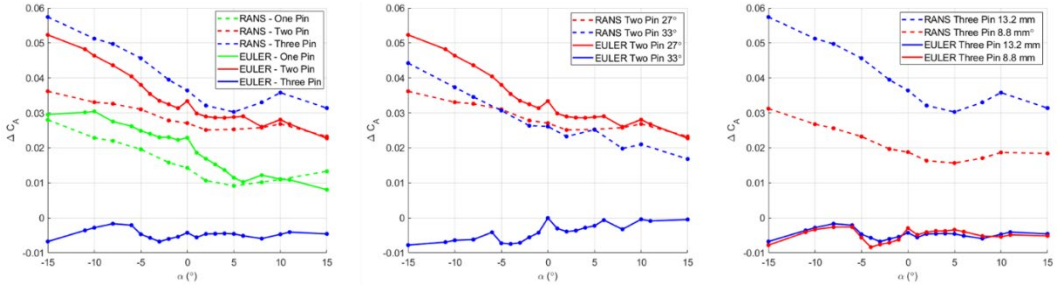

Figure 29. ΔC_A **calculated from RANS and Euler simulations for the one-pin, two-pin, 27°, and three-pin, 13.2-mm configurations (left); the two, 2-pin configurations (middle); and the two, 3-pin configurations (right).**

Analyzing the C_m plots in Figure 26, the vehicle is statically stable for the center of gravity chosen for $\alpha < -2$ and $\alpha > 2$. At low α there is a relatively small degree of static instability. Similar to Figure 25, Figure 27 shows both the Euler and RANS simulations produce a smaller ΔC_m contribution from the pin effectors as α

increases. The qualitative observation was made in the previous Section 4.1.1 that the high pressures produced by the pins would likely offset the low pressures behind the pins. The coefficient data integrates all surface pressures and the pin effector performance at high α can now be quantified. For Euler simulations, all configurations maintain approximately 50% ΔC_m magnitude at $\alpha = 15°$ compared to $\alpha = 0°$. For RANS simulations, the one- and three-pin configurations maintain over 70% ΔC_m magnitude up to $\alpha = 15°$ compared to $\alpha = 0°$. The two-pin configurations are different. For the two-pin configurations, ΔC_m magnitude degrades appreciably to 50% for the two-pin, 27° configuration and to 25% for the two-pin, 33° configuration. Again, focusing on one-pin, two-pin, 27°, and three-pin, 13.2-mm configurations (left plot in Figure 27), the Euler simulation overpredicts the ΔC_m contribution from the pin effectors compared with the RANS simulation and the overprediction is exacerbated at negative α. This overprediction is also greater comparing the two-pin, 27° configuration with the one-pin configuration and comparing the three-pin, 13.2-mm configuration with the two-pin, 27° configuration.

Focusing on the comparison between the two, 2-pin configurations (middle plot in Figures 25 and 27), the subtle differences observed previously correspond to negligible differences in ΔC_N and ΔC_m values. Focusing on the comparison between the two, 3-pin configurations (right plot in Figure 25 and Figure 27), the flow-field differences previously noted correspond to observable differences in ΔC_N and ΔC_m values. Coincidentally, the ΔC_N and ΔC_m values for the three-pin, 8.8-mm configuration are roughly equivalent to the ΔC_N and ΔC_m values for the two-pin, 27° configuration. It appears that a reduction in the height of three-pin effectors by 4.4 mm corresponds to the removal of a pin effector with a height of 13.2 mm; in both cases, there is a one-third reduction in frontal area. Analyzing Figures 25 and 27, both Euler and RANS simulations capture the decrease in the ΔC_N and ΔC_m contribution from the pin effectors as α increases for all configurations. Euler simulations significantly overpredict the RANS simulations, which may lead to a lack of control authority if pins are used for maneuverability.

Analyzing the C_A plots in Figure 28, there is a predictable trend of increasing C_A as more pin effectors are added to the baseline configuration. This is true at all α considered in this investigation. However, sensible C_A data was not obtained for three configurations from Euler simulations. The C_A data obtained is not sensible because the three configurations should have higher drag compared to the baseline, but the drag is lower. However, this is not problematic because C_A data from Euler simulations is not reliable and has limited utility. RANS results are reliable, and as expected, show an increase in C_A and ΔC_A with an increasing number of pins

(Figures 28 and 29). The same trends observed by analyzing Figures 25 and 27 are seen in Figure 29.

It is clear from the paragraphs above that the Euler CFD generally overpredicts the ΔC_N, ΔC_m, and ΔC_A, compared with RANS solutions and it gets worse at large negative α. These incremental force and moment coefficients are also nonlinear with respect to angle of attack. The nonlinear effects must be correctly accounted for if additional pins are added to improve aerodynamic performance and maneuverability.

An aerodynamic performance metric for the pitch control investigation is determining a pin effector configuration equivalent tail-flap deflection angle. For $\alpha = 0°$, the ΔC_N and ΔC_m values generated by the pin effectors are interpolated as a function of C_N and C_m corresponding to tail-flap deflection, δ, to calculate an equivalent δ value the pin effectors are generating. This aerodynamic performance metric was explained and analyzed in previous investigations.[16,17] The equivalent moment flap deflection is a degree less than the equivalent normal force deflection. Analyzing the equivalent tail-flap deflection, δ, values for the one-pin, two-pin, 27°, and three-pin, 13.2-mm configurations (Figure 30, top row), each additional pin effector seems to add roughly $\delta = 1°$ according to the RANS data and slightly more according to the Euler data. Comparing the taller three-pin, 13.2-mm configuration to the shorter three-pin, 8.8-mm configuration we see that the reduction in height corresponds to approximately $\delta = 2°$. As previously described, this reduction in height seems to correspond to the removal of a pin effector. In all cases, the Euler simulations significantly overpredict the equivalent δ compared with the RANS simulations.

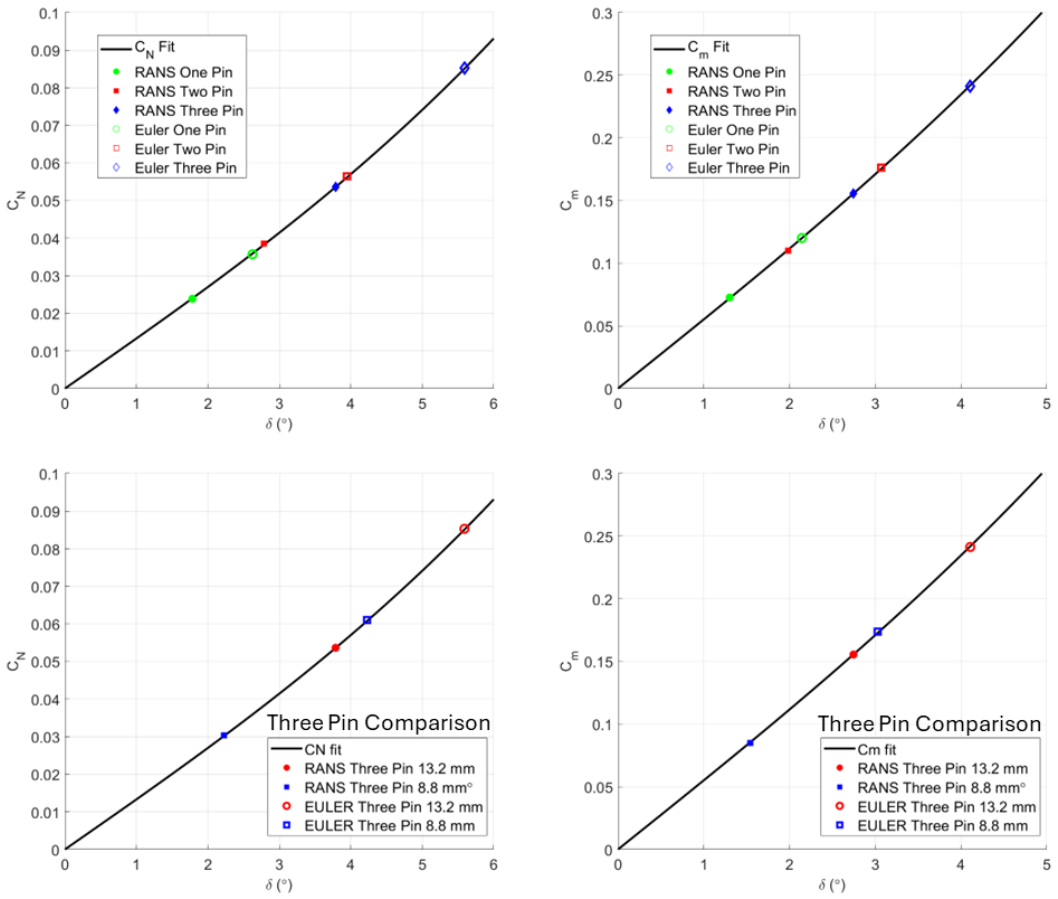

Figure 30. Equivalent tail-flap deflection for $\alpha = 0°$ calculated using C_N and C_m for four pin effector configurations (two-pin, 33° excluded). The top row compares RANS and Euler results for the one-pin, two-pin, 27°, three-pin, 13.2-mm configurations; and the bottom row compares the two 3-pin configurations with different heights.

This analysis of pin effector pressure distributions, aerodynamic performance, and comparison against a conventional mechanism for aerodynamic control demonstrates the capability of Euler CFD to handle quick design analysis of these types of variant configurations. However, for better understanding of the flow physics associated with these pin effector designs and more accurate predictions of the aerodynamic performance, RANS CFD would be more appropriate. Euler CFD can calculate the appropriate shock structure geometry, magnitude and trends of C_N and C_m, and provide insight on ΔC_N and ΔC_m. The comparison against tail-flap control was made to quickly relate the pin effector loads to a conventional control method. These variant configurations could be compared against tail-flap control in trajectory simulations for given mission parameters to assess potential advantages and disadvantages. However, using Euler simulation results could lead to overprediction of their absolute effectiveness.

4.2 Roll Control Simulations

For roll control, the previously computed baseline configuration and four pin effector configurations were considered. The results of the roll control investigation are separated into two subsections. Subsection 4.2.1 shows computed surface pressure contours on the projectile in immediate proximity to the pin effectors. Subsection 4.2.2 presents the results for pin effector aerodynamic roll performance obtained from both the Euler and RANS simulations.

4.2.1 Surface Pressure Contour Analysis

Although roll computations were for a range of angles of attack, $-15° < \alpha < 15°$ using Euler and RANS CFD techniques, qualitative results are now presented for a few representative cases: $\alpha = 0°$, 5°, and 8° for the 0.126 cal., four-pin, 27° roll configuration only.

Figures 31–35 show the computed surface pressure contours in the aft end of the projectile in the vicinity of the pin obtained from RANS solutions. Figure 31 shows computed surface pressures in a side view at $\alpha = 0°$. High pressures are shown in red and low in blue. As expected, a high-pressure region is clearly shown in front of the pin and also on the fin next to the pin due to strong shock interactions resulting from the pin shock impinging on the fin. It is interesting that shock-interaction effect extends all the way across the main body to the other adjacent fin and the rear flap too. Figures 32 and 33 show computed surface pressures in the x-y and x-z planes, respectively, at $\alpha = 5°$. Figure 32 shows generally weaker shock interactions on the lee side (left picture) and stronger interactions on the wind side (right picture). The same is true of the surface pressure contours for the two side views (Figure 33). With increase in angle of attack to α=8°, computed surface pressures are lower again on the lee side and stronger on the wind side (see Figure 34). Again, the contrast is more easily seen between the two side views at $\alpha = 8°$ in Figure 35.

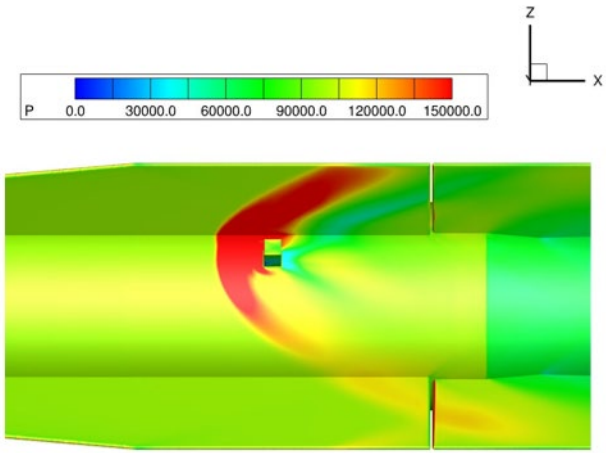

Figure 31. Computed surface pressure contours showing detail near the pin effectors from RANS simulations for the four-pin, 27° roll configuration at α = 0°, x-z view.

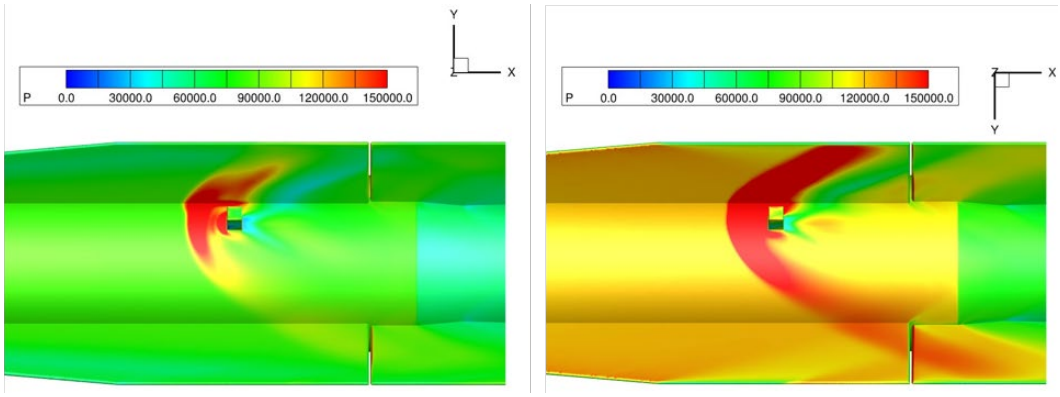

Figure 32. Computed surface pressure contours showing detail near the pin effectors from RANS simulations for the four-pin, 27° roll configuration at α = 5°, x-y view from top, lee side (left) and x-y view from bottom, wind side (right).

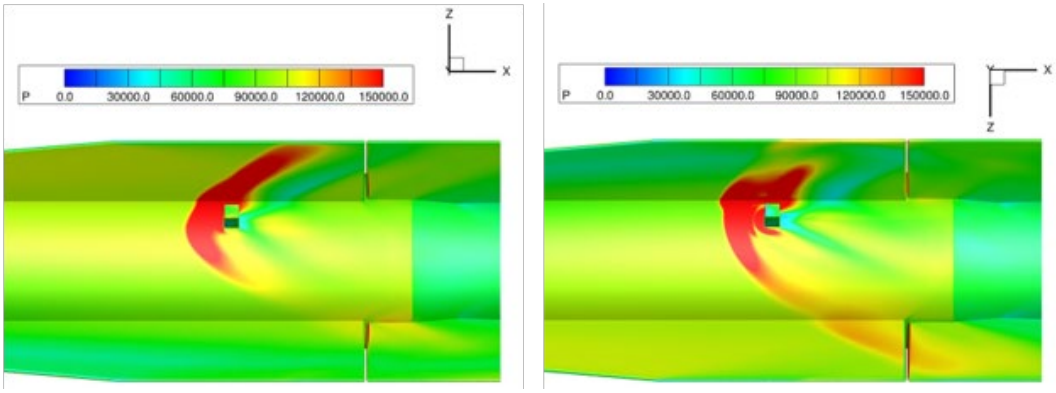

Figure 33. Computed surface pressure contours showing detail near the pin effectors from RANS simulations for the four-pin, 27° roll configuration at α = 5°, x-z or side view (left) and x-z side view rotated 180° (right).

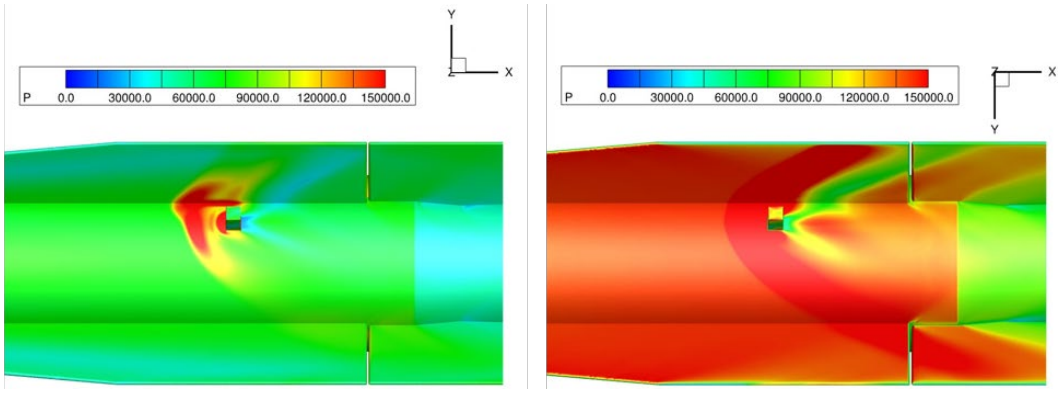

Figure 34. Computed surface pressure contours showing detail near the pin effectors from RANS simulations for the four-pin, 27° roll configuration at α = 8°, x-y view from top, lee side (left) and x-y view from bottom, wind side (right).

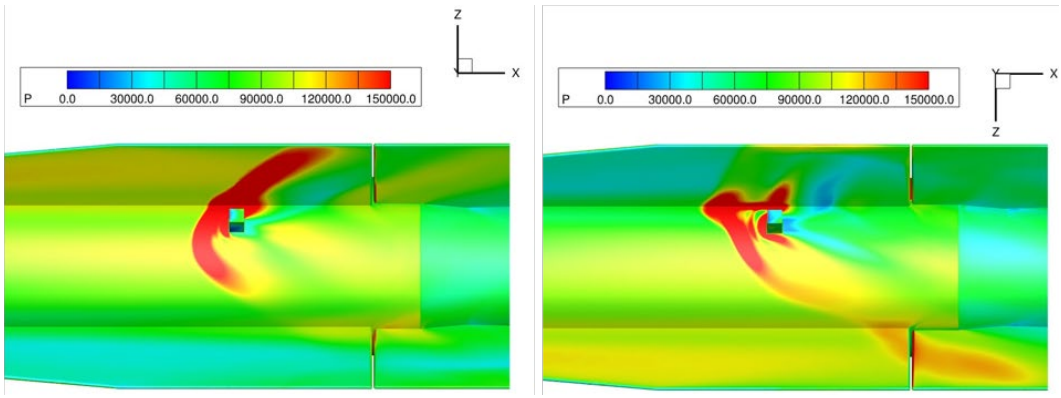

Figure 35. Computed surface pressure contours showing detail near the pin effectors from RANS simulations for the four-pin, 27° roll configuration at α = 8°, x-z or side view (left) and x-z side view rotated 180° (right).

A few representative cases are now presented from the Euler solutions at same, α = 0°, 5°, and 8° for the 0.126-cal., four-pin, 27° roll configuration. Figures 36–38 show the computed surface contours in the vicinity of the pins at α = 0°, 5°, and 8°, respectively. Figure 36 shows computed surface pressures in a side view at α = 0°. Again, high pressures are shown in red and low in blue. Similar to the RANS solution, it clearly shows a high-pressure region in front of the pin and also in the fin next to the pin due to strong shock interactions. It also shows the shock-interaction effect extending all the way across the main body to the other adjacent fin and the rear flap as was the case for the RANS solution. However, compared to the RANS solution (Figure 31), Euler results show a smaller region of high pressure in front of the pin and also on the fin adjacent to the pin. The same trend continues at angles of attack, α = 5° (Figure 37) and α = 8° (Figure 38). It seems the shock-interaction effect on the other fin is somewhat increased as seen in these figures compared with the RANS solutions (Figures 33 and 35).

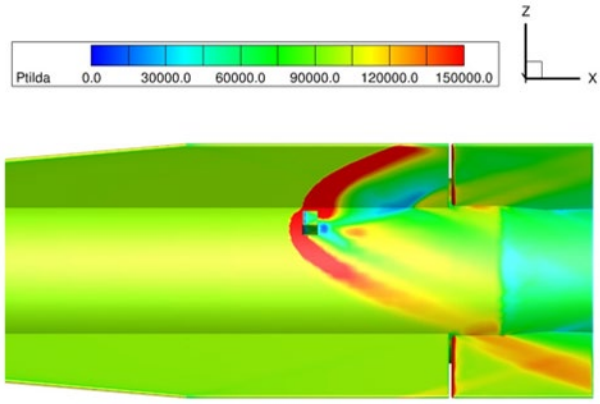

Figure 36. Computed surface pressure contours showing detail near the pin effectors from Euler simulations for the four-pin, 27° roll configuration at α = 0°, x-z view.

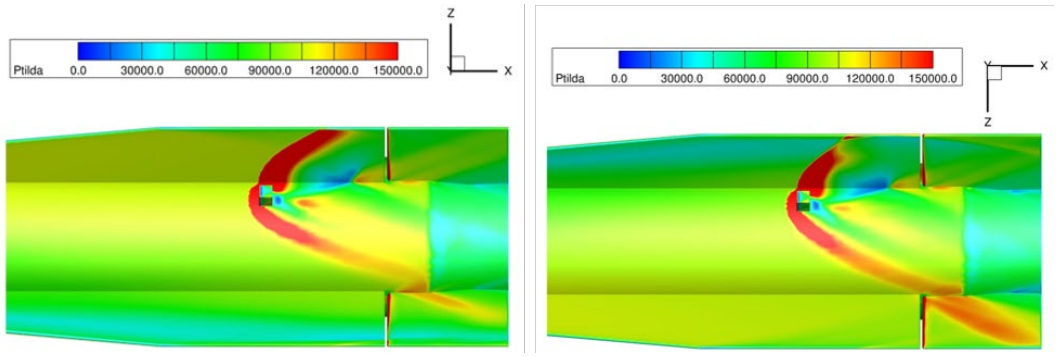

Figure 37. Computed surface pressure contours showing detail near the pin effectors from Euler simulations for the four-pin, 27° roll configuration at α = 5°, x-z or side view (left), and x-z side view rotated 180° (right).

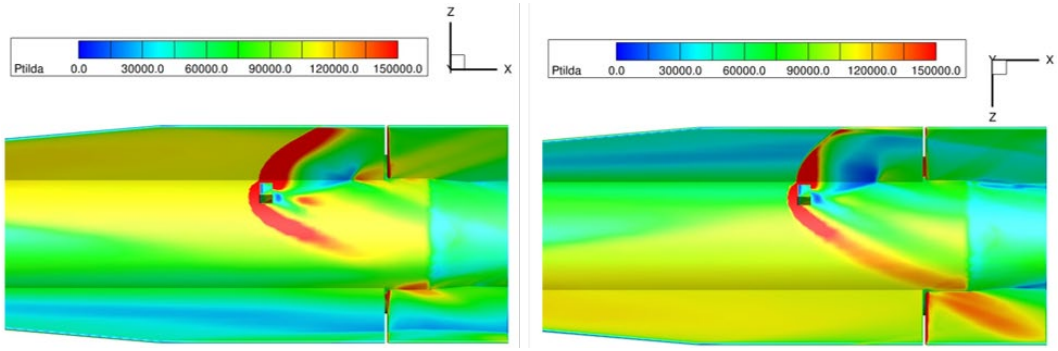

Figure 38. Computed surface pressure contours showing detail near the pin effectors from Euler simulations for the four-pin, 27° roll configuration at α = 8°, x-z or side view (left), and x-z side view rotated 180° (right).

As discussed, differences are seen in the computed surface contours between the RANS and Euler solutions even at 0° angle of attack. Figures 39 and 40 show comparisons of RANS and Euler computed surface pressure contours in the lee side for the four-pin, 27° roll configuration at α = 5° and 8°, respectively. Both figures show a larger region of high pressures in front of the pin with the RANS solution;

however, with no shock-boundary interactions, the shocks are sharper, a lot less diffused, and more prominent at both fins, body itself, and rear flaps for the Euler solution.

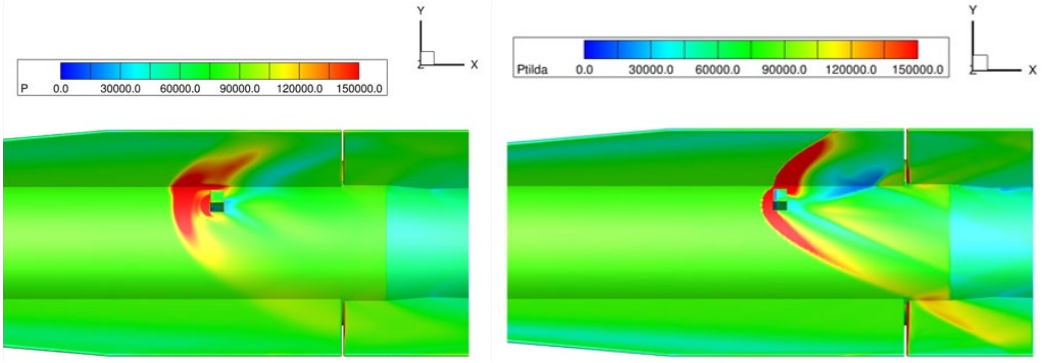

Figure 39. Computed surface pressure contours on the lee side showing detail near the pin effectors for the four-pin, 27° roll configuration at α = 5°, RANS (left) and Euler (right).

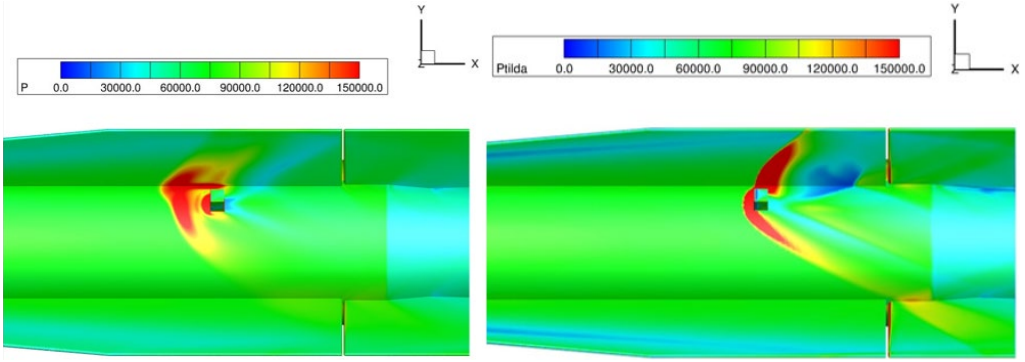

Figure 40. Computed surface pressure contours on the lee side showing detail near the pin effectors for the four-pin, 27° roll configuration at α = 8°, RANS (left) and Euler (right).

4.2.2 Aerodynamic Roll Performance

The primary aerodynamic metric that is of interest here is the roll moment coefficient, C_l for roll control. However, for completeness, all coefficients are presented for the four-pin, 27° and the four-pin, 33° roll configurations. It includes three force coefficients (axial, side, and normal); C_A, C_S, and C_N and also three moment coefficients (roll, pitching, and yawing); C_l, C_m, and C_n. For roll control, the taller pin with a height of 0.126 cal. was used in both RANS and Euler computations. A smaller pin with a reduced height of 0.084 cal. was also used in the Euler calculations to see if it still is effective for roll control.

The force coefficients are shown in Figures 41–43 as a function of angle of attack. Figure 41 shows the C_A variation with angle of attack. Both RANS and Euler results show similar trends with angle of attack; however, magnitudes are very different even for the baseline configuration with no pins. Since RANS results are more

reliable, we will focus on these results. RANS results show an increase in C_A with the pins (compared to the baseline) of about 15%–19% across the whole range of angle of attack from $-15° < \alpha < 15°$ with the largest increase at $\alpha = 0°$. Also, the increase in drag due to the pins is almost the same for both the four-pin, 27° and the four-pin, 33° roll configurations; just a very slight increase for the four-pin, 27° compared with the four-pin, 33° roll configuration. Figure 42 shows the variation of the side force coefficient, C_S with angle of attack. The location of the pins (Figure 30) results in flow field that cancels out left and right sides only at 0° angle of attack and C_S, is zero. For other angles of attack, the flow field is different (see Figures 33 and 35) and it produces a net side force. Both RANS and Euler results show a highly nonlinear variation of C_S with angle of attack. There are however some differences in the predicted C_S between RANS and Euler for the different roll configurations especially at angles of attack larger than 5°. As expected, and as seen in Figure 43, there are only very minor changes in the normal force coefficient among all configurations and between RANS and Euler predictions similar to what was observed with the pitch control discussed earlier. Plotting the delta coefficients would likely show greater differences. However, that is not the focus of this section.

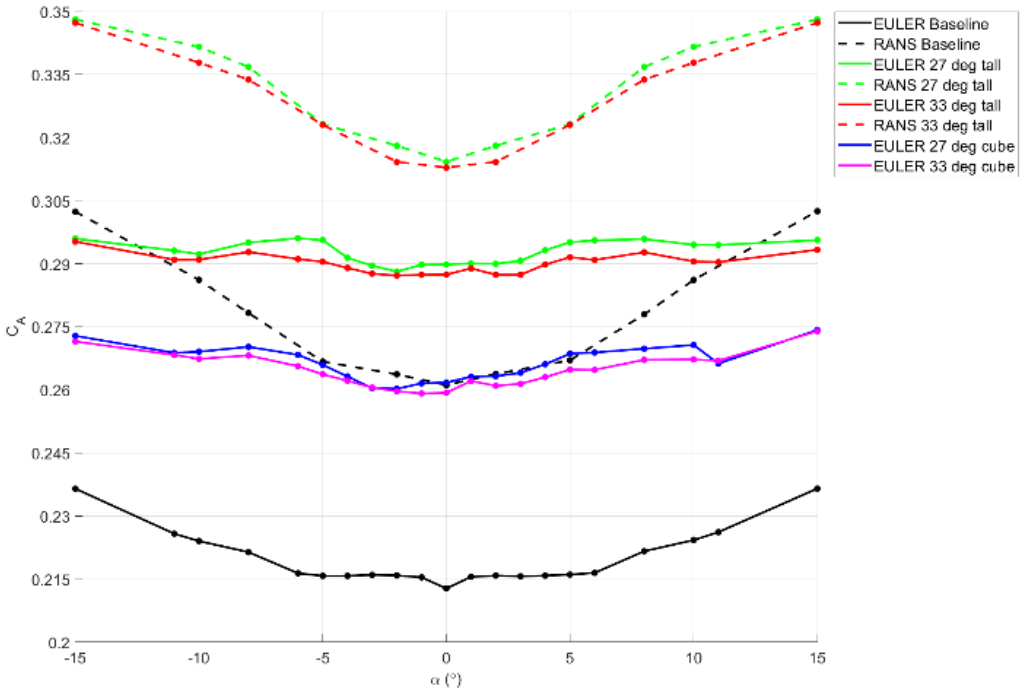

Figure 41. Comparison of computed C_A from RANS and Euler simulations for the four-pin, 27°, the four-pin, 33°, 0.126-cal. (tall) roll configurations.

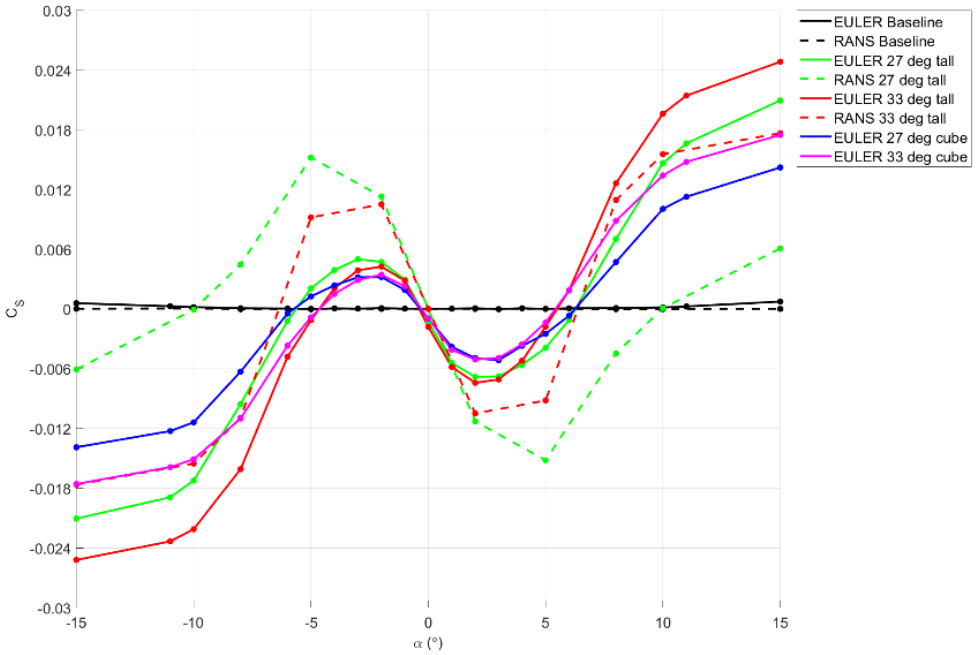

Figure 42. Comparison of computed C_S from RANS and Euler simulations for the four-pin, 33°, 0.126-cal. (tall) roll configurations.

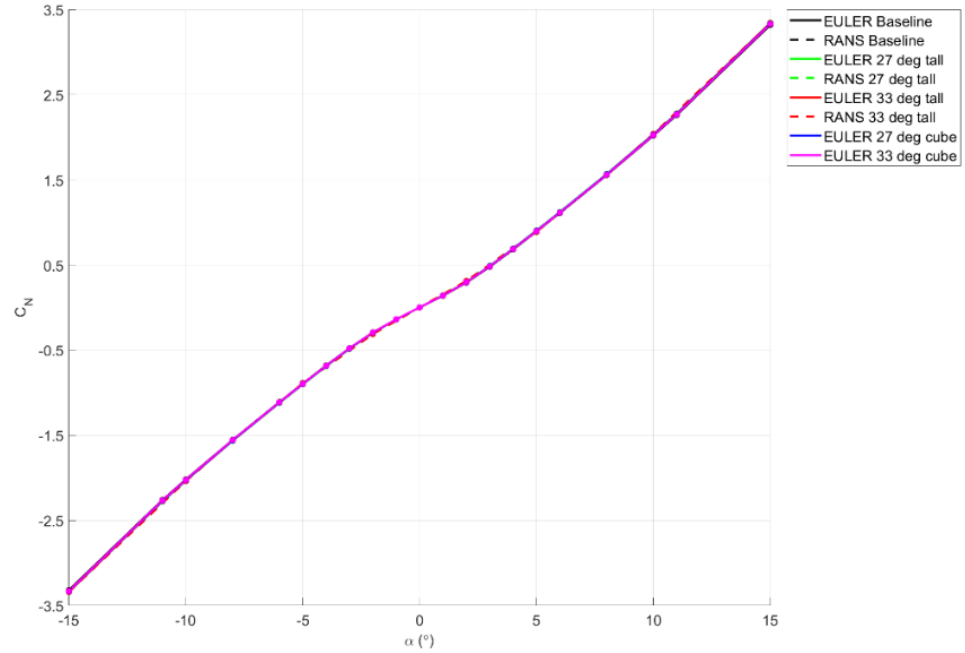

Figure 43. Comparison of computed C_N from RANS and Euler simulations for the four-pin, 33°, 0.126-cal. (tall) roll configurations.

The moment coefficients are shown in Figures 44–46 as a function of angle of attack. Of primary interest is the aerodynamic roll moment coefficient, C_l (defined as positive rolling clockwise looking from the back), and is shown in Figure 44 for both the four-pin, 27°, and the four-pin, 33° roll configurations with both 0.126-cal. (tall) and 0.084-cal. (cube) pins. Both RANS and Euler show similar trends; predicted C_l is nearly symmetric about 0° angle of attack. Both methods predict the roll moment coefficient to be almost linear at low angles of attack ($\alpha \leq$ 5°) and more nonlinear at higher angles of attack. With the Euler simulations, the four-pin, 33° configuration seem to produce more roll moment than the four-pin, 27° roll at all angles of attack up to 11° with substantial gain near $\alpha = 0°$, indicating placing the pin closer to the fin may be a better choice, if the Euler solution is trusted. Euler solutions were also obtained, and C_l was computed from these solutions for both the four-pin, 27°, the four-pin, 33° roll configurations with a smaller 0.084-cal. high pin (labeled as cube in these figures since the height is the same as the width and depth). Compared with the same roll configuration with a pin height of 0.126 cal., reduced height pin (0.084 cal.) reduces the roll moment some as expected; however, they can still provide some roll control.

The RANS result for the four-pin, 27° roll configuration is shown as a green dotted line and the RANS result for four-pin, 33° configuration in a red dotted line. At lower angles of attack ($|\alpha| \leq 4°$), four-pin, 27° roll configuration produces a little more negative roll moment than the four-pin, 33° roll configuration while the four-pin, 33° roll configuration provides more roll moment than the four-pin, 27° configuration between $|\alpha| \leq 4°$ and 7°. At higher angles of attack between ($|\alpha| =$ 7° and 14°), the four-pin, 27° roll configuration again produces more roll moment than the four-pin, 33° roll configuration. With RANS, the difference between the predicted values of C_l between the two roll configurations is large at higher angles of attack ($|\alpha| \geq 9°$) and smaller at lower angles of attack, while the opposite seems to be true in the Euler predictions. In general, Euler results overpredict C_l quite a bit compared with RANS. This large discrepancy can clearly be attributed to shock-/boundary-layer interaction effects. RANS, which includes shock-/boundary-layer interactions, has a significant effect on the flow structures/asymmetries and flow interactions over the body as well as the fins/flaps. As a result, at lower angles of attack ($\alpha \leq 5°$) for the four-pin, 27° roll configuration and $\alpha \leq 4°$ for the four-pin, 33° roll configuration, RANS actually predicts negative roll moment. It is somewhat counterintuitive in the sense one would have expected higher pressure on the fin adjacent to the pin to have produced a clockwise positive roll moment.

As will be discussed later, the integrated forces on the flaps, due to the pin shock impingement crossing the body due to the pin being as far forward as it is, causes the roll reversal. Thus, when the Euler method overpredicts C_l quite a bit as

compared with RANS, it also predicts the roll moment in the opposite direction (signs are opposite to that of RANS near α = 0°), due to the small values. The pitching moment coefficient and yawing moment coefficient are shown in Figures 45 and 46 as a function of angle of attack. The asymmetry in the flow field between the wind side and the lee side is small at very low angles of attack and gets more prominent at higher angles of attack, which leads to some differences in C_m (Figure 45). As seen in Figure 46, the trend with angle of attack is similar but opposite in sign to C_n, again resulting from the flow asymmetries between the left and the right sides.

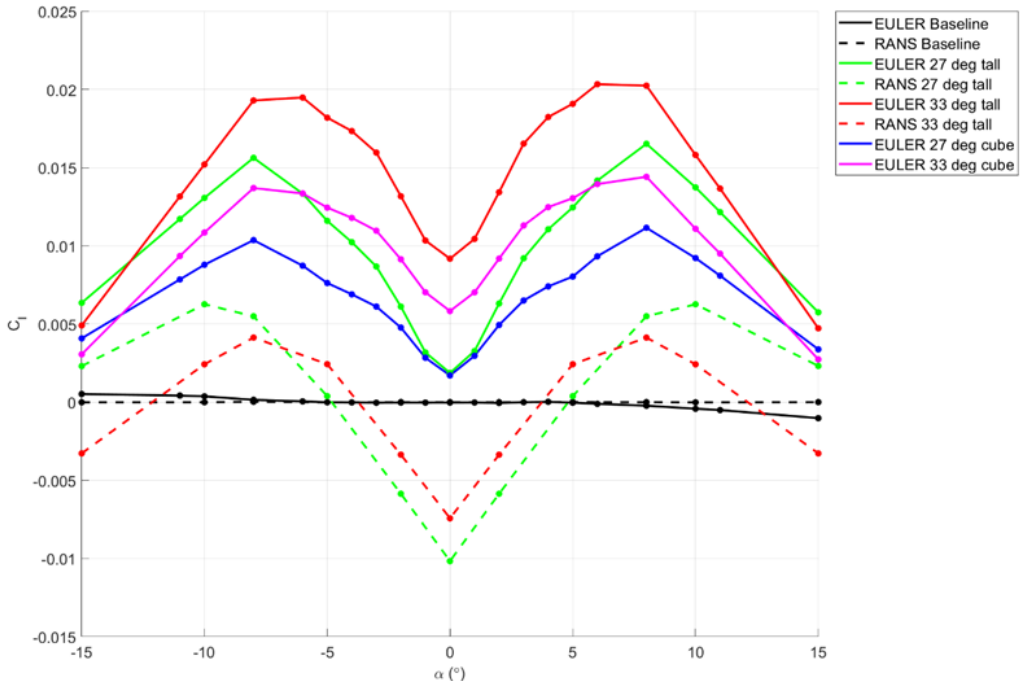

Figure 44. Comparison of computed C_l from RANS and Euler simulations for the four-pin, 27°, the four-pin, 33°, 0.126-cal. (tall) roll configurations.

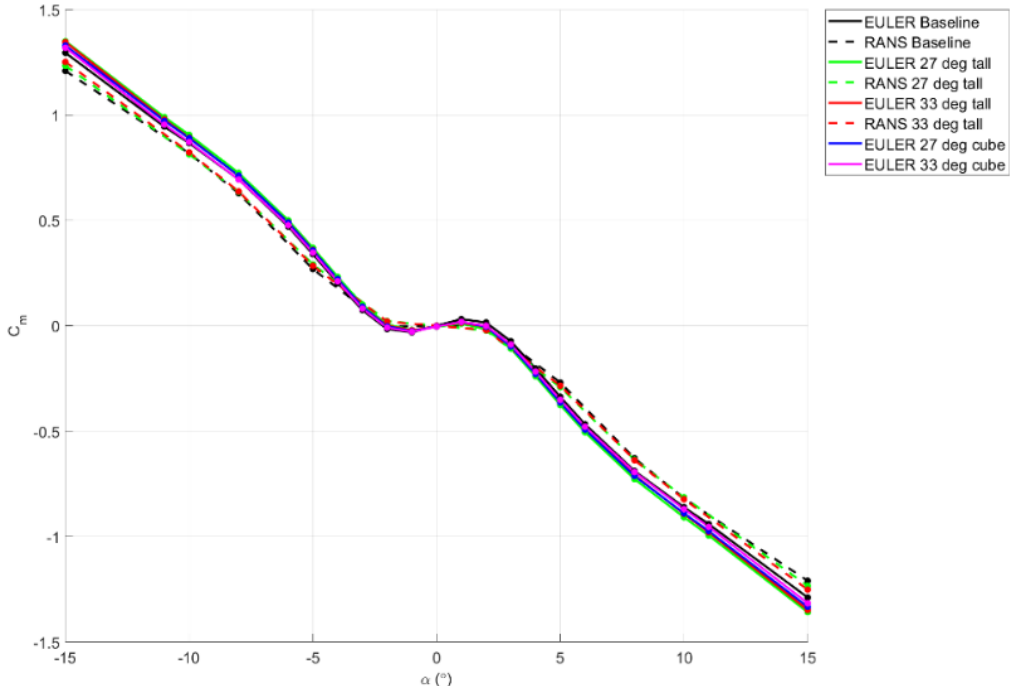

Figure 45. Comparison of computed C_m from RANS and Euler simulations for the four-pin, 27°, the four-pin, 33°, 0.126-cal. (tall) roll configurations.

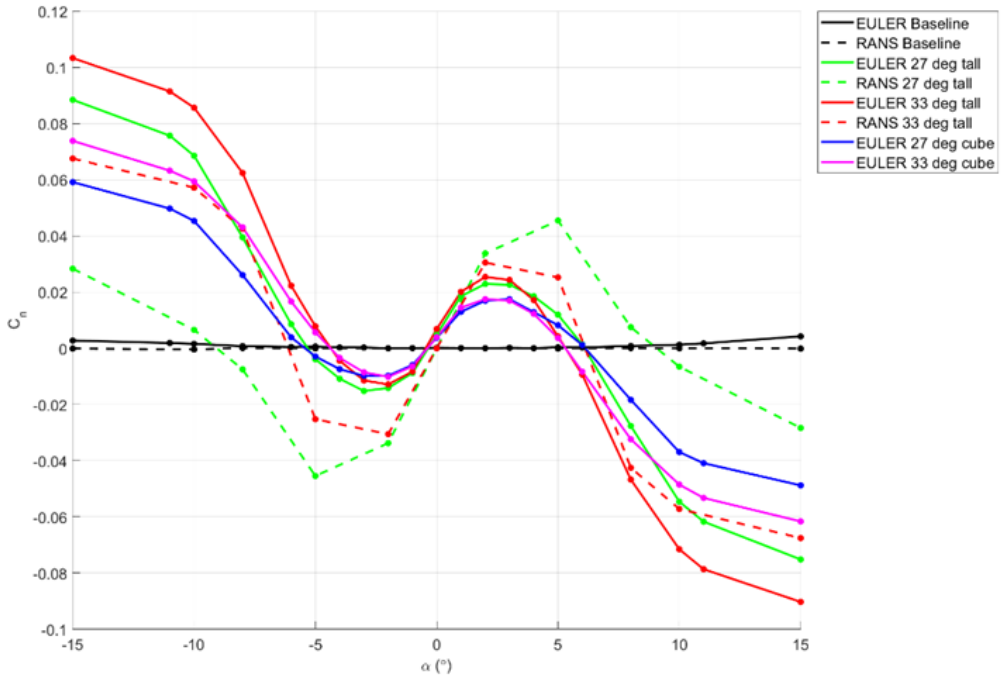

Figure 46. Comparison of computed C_n from RANS and Euler simulations for the four-pin, 27°, the four-pin, 33°, 0.126-cal. (tall) roll configurations.

To get a little more insight into the roll moment predictions and based on the C_l discussion shown in Figure 44, three representative cases, $\alpha = 0°$, 5°, and 8°, for the four-pin, 27° roll configuration were selected. For these cases, C_l was obtained for each body component separately from the computed RANS solution. Table 1 shows the detailed contribution of each of the body components to total C_l.

Table 1. Details of body component contributions to the roll moment coefficient, C_l, from RANS simulations for the 0.126-cal. (tall), four-pin, 27° roll configuration as a function of angle of attack.

Angle of attack/ C_l components	0	5	8
front body	–2.42E-04	–2.57E-04	–2.69E-04
rear body	–3.39E-06	–3.29E-06	5.77E-06
fin1	6.42E-03	–6.49E-02	–9.97E-02
fin2	6.42E-03	7.22E-02	1.10E-01
fin3	6.42E-03	1.19E-01	2.02E-01
fin4	6.42E-03	–1.02E-01	–1.83E-01
flap1	–8.58E-03	–1.38E-02	–2.17E-02
flap2	–8.58E-03	3.19E-03	9.83E-03
flap3	–8.58E-03	8.76E-03	2.62E-02
flap4	–8.58E-03	–2.07E-02	–3.78E-02
pin1	–3.05E-04	–1.51E-04	2.86E-04
pin2	–3.07E-04	–1.76E-04	5.98E-04
pin3	–3.07E-04	–2.49E-04	–2.86E-04
pin4	–3.58E-04	–3.65E-04	–7.27E-04
Total C_l	–1.02E-02	3.84E-04	5.49E-03

As seen in Table 1, contributions from the front body, rear body, and all four pins are rather small (~15%) and counteract the roll moment generated by the flaps (i.e., the opposite direction). The main contributors to the total roll moment coefficient are the fins and the flaps. At 0° angle of attack, contribution from each fin is the same as expected; the contribution of each flap is also the same. However, the fins produce a positive roll moment whereas the flaps produce a negative roll moment (with a larger magnitude) resulting in a net negative C_l at $\alpha = 0°$. The net negative roll moment produced by the flaps here is a direct result of the flow interactions of each pin affecting the flow field on the rear flap of the fin away from the pin. With increase in angle of attack to 5° and 8°, fins and flaps remain the largest contributors. At angles of attack, flow asymmetries develop due to both the flow and the interaction effects, which contribute to the varying roll moment contributions from the fins and flaps. As seen in Table 1, fins and flaps on the wind side seem to have larger flow interaction effects resulting in larger magnitudes in C_l than the ones on the lee side. The total roll moment coefficient, C_l is shown in the last line of the table and matches the values shown in Figure 44.

Unlike pitch control where the flow interactions are more straightforward (no flow asymmetry between the left and right sides), for roll control, the location of the pin

itself creates additional asymmetrical flow interactions between the top and bottom, and between the left and right sides of the projectile. As discussed above, the Euler method does not include shock-/boundary-layer interactions, is unable to predict all asymmetric flow interactions properly, and fails to predict C_l correctly especially near 0° angle of attack. Therefore, for better understanding of the flow physics associated with these pins and more accurate predictions of the aerodynamic performance, RANS CFD would definitely be more appropriate for roll control. For better roll control, further investigation is needed to look at alternate pin locations, arrangements, and other pin shapes.

5. Conclusions

In this investigation the effect of pins was studied for both pitch and roll control of a high-speed vehicle at a supersonic speed, $M = 3$, over a range of angles of attack, $-15° < \alpha < 15°$, using both Euler and RANS techniques.

For pitch control, Euler simulations and RANS simulations were conducted to analyze a baseline configuration of a high-speed vehicle and five variant configurations that use pin effectors for a pitch maneuver. The five variant configurations are the one-pin, two-pin – 27°, two-pin –33°, and three-pin, all with pin height of 0.126 cal., and the three-pin with a smaller height, 0.084 cal. Computed surface pressure contours show how the high-pressure regions both in front of and behind the pin effectors decrease in size and intensity as α increases. These high-pressure regions generated around the pin effectors behind the center of pressure generate a negative C_N contribution and a positive C_m contribution. Computed results show important differences comparing the calculated shock structure in the Euler and RANS simulations, which arise due to the inclusion of viscous terms in the Navier–Stokes equations. The inclusion of viscosity enables RANS simulations to account for more complicated phenomenon, such as shock-boundary layer interaction and the impact of body vortex roll-up generated by the airframe of the projectile.

In terms of aerodynamic performance, Euler and RANS simulations seem to show reasonable agreement in both C_N and C_m. However, in looking at the more important or critical incremental forces and moments, Euler simulations overpredict both the ΔC_N and ΔC_m contributions generated by the pin effectors. This overprediction by the Euler simulations is exacerbated at negative α. Both Euler and RANS simulations showed the variant configurations maintained appreciable fractions of ΔC_m generated by the pin effectors at high α, demonstrating the pin effectors maintain reasonable effectiveness on the lee side in the shadow of the vehicle. This investigation also showed the limitations in Euler CFD analyzing

C_A and ΔC_A. The aerodynamic performance assessed for pitch control was found to be nonlinear with the most prominent effects present at negative α. Collectively, the results and analysis in this investigation for pitch control do show differences among Euler and RANS data (in some cases Euler overpredicts the delta values by nearly 100%). With that in mind, Euler technique can still be used for all pin effector configurations for quick design analysis where relative performance is being evaluated. However, for better understanding of the flow physics associated with these pin effector designs and more accurate predictions of the aerodynamic performance, RANS CFD would be a better option.

For roll control, baseline and three other configurations with four pin effectors were considered in this study for roll control of the vehicle. In general, Euler results overpredict C_l quite a bit compared with RANS. This large discrepancy can clearly be attributed to shock-/boundary-layer interaction effects. RANS, which includes shock-/boundary-layer interactions, has a significant effect on the flow structures/asymmetries and flow interactions over the body as well as the fins/flaps. In particular, the flow interactions from the pin have a strong effect on the flap away from the pin and hence, on the roll moment produced. RANS captures this effect properly, but Euler results fail to predict C_l correctly and has roll moment in the opposite direction especially near 0° angle of attack, due to its small magnitude. As such, the Euler method may not be an appropriate tool for accurate prediction of roll control and should be used with caution. Clearly, RANS can take into account all asymmetric flow interactions properly and would be a better choice for accurate prediction of roll moment for roll control.

The pin arrangement studied in this investigation for both pitch control and roll control was not optimized. In future work, more complex arrangements of pin effectors with more pins at either the same axial location or at multiple axial locations simultaneously can be investigated to optimize control authority for pitch control. For roll control, other rear locations or changes in pin shapes could be considered for improved roll control. Future research will extend this analysis to higher Mach numbers, unsteady effects such as deploying the pin effectors, open-loop simulations, and fully coupled CFD/RBD trajectory simulations.

6. References

1. Sahu J, Fresconi F, Heavey K. Control performance, aerodynamic modeling and validation of coupled simulation techniques for guided projectile roll dynamics. Paper presented at: AIAA Aviation 2014 Forum; 2014 June; Atlanta, GA.

2. Coyle CJ, Silton S. CFD aerodynamic characterization of a high maneuverability airframe. Paper presented at: 33rd AIAA Applied Aerodynamics Conference; 2015 June 22–26; Dallas, TX. AIAA Paper No.: 2015-3015.

3. Sahu J, Fresconi F. Flight behaviors of a complex projectile using a coupled CFD based simulation technique: open-loop control. Paper presented at: AIAA SciTech Forum and Exposition; 2016 Jan; San Diego, CA.

4. Sahu J, Fresconi F. Flight behaviors of a complex projectile using a coupled CFD based simulation technique: closed-loop control. Paper presented at: AIAA Aviation Forum; 2016 June; Washington, D.C.

5. Silton S, Sahu J, Fresconi F. Comparison of uncoupled and coupled CFD-based simulation techniques for the prediction of the aerodynamic behavior of a complex projectile. Paper presented at: AIAA Aviation Forum; 2016 June; Washington, D.C.

6. Youn E et al. Aerodynamic analysis of a high maneuverability airframe utilizing magnetic resonance velocimetry and Reynolds-Averaged Navier–Stokes simulations. Paper presented at: 55th AIAA Aerospace Sciences Meeting; 2017 Jan 9–13; Grapevine, TX. Paper No.: AIAA 2017-1662.

7. Burchett B, Sahu J, Gruenwald B. Tuning flap control authority from high fidelity, coupled CFD/RBD virtual fly-outs. DEVCOM Army Research Laboratory (US); 2022 Sep. Report No.: ARL-TR-9543.

8. Sahu J, Gruenwald BC, Burchett BT. Adaptive control validation using a MATLAB-based CFD/RBD coupled simulation. DEVCOM Army Research Laboratory (US); 2022 Apr. Report No.: ARL-TR-9433.

9. Bryson JT, Vasile JD, Paul JL, Sahu J, Gruenwald BC. Modeling and flight dynamics of a projectile with nonlinear, roll-dependent aerodynamics. DEVCOM Army Research Laboratory (US); 2020 Sep. Report No.: ARL-TR-9047.

10. Massey CK et al. Mechanical actuators for guidance of a supersonic projectile. Paper presented at: 23rd AIAA Applied Aerodynamics Conference; 2005 June. AIAA Paper No.: 2005-4970.

11. Massey CK, Guthrie BK, Silton IS. Optimized guidance of a supersonic projectile using pin based actuators. Paper presented at: 23rd AIAA Applied Aerodynamics Conference; 2005 June. AIAA Paper No.: 2005-4966.

12. Massey CK, Silton IS. Testing the maneuvering performance of a Mach 4 projectile. Paper presented at: 24th Applied Aerodynamics Conference; 2006 June. AIAA Paper No.: 2006-3649.

13. Silton IS, Massey CK. Investigation of actuator performance for guiding supersonic projectiles. J Spacecr Rocket. 2008;45(3).

14. Massey CK et al. Mechanical actuators for guidance of a supersonic projectile. J Spacecr Rocket. 2008;45(4).

15. Massey CK, Silton IS. Combining experimental data, computational fluid dynamics, and six-degree of freedom simulation to develop a guidance actuator for a supersonic projectile. J Aerosp Eng. 2008;223(Part G).

16. Bell M, Watterson KJ, Lisk D. A numerical study into a local protuberance interaction with a fin on a supersonic projectile. Paper presented at: 47th AIAA Aerospace Sciences Meeting; 2009 Jan. AIAA Paper No.: 2009-1092.

17. Cler DL, Carson R, Dillon R, Costello M. Flow manipulation of a fin on a flat plate interaction in high-speed flow by means of micro flaps. Benet Laboratories (US); 2009. Report No.: ADA588653.

18. Dykes J et al. Use of microspoilers for control of finned projectiles. J Spacecr Rocket. 2012;49(6).

19. Sahu J, Heavey KR. Parallel CFD computations of projectile aerodynamics with a flow control mechanism. Comput Fluids. 2013;88:678–687.

20. Scheuermann E et al. Aerodynamic characterization of a microspoiler system for supersonic finned projectiles. J Spacecr Rocket. 2015;52(1).

21. Sahu J. CFD simulations of a finned projectile with microflaps for flow control. In: Proceedings of the 27th International Conference on Parallel CFD; 2015 May; Montreal, Canada.

22. Sahu J. CFD simulations of a finned projectile with microflaps for flow control. J Aerosp Eng. 2017;2017:4012731.

23. Leonard A, Rogers J, Sahu J. Aerodynamic optimization of microspoiler actuators for guided projectiles. J Spacecr Rocket. 2017;54(6).

24. Celmins I. Design and evaluation of an electromechanical actuator for projectile guidance. Army Research Laboratory (US); 2007 Sep. Report No.: ARL-MR-0672.

25. Dooroo K et al. Actuator design and flight testing of an active microspoiler-equipped projectile. J Dyn Syst Meas Control. 2017;139:111002.

26. Chang S, Li D. Aerodynamic coefficients of a microspoiler for spin-stabilized projectiles. J Spacecr Rocket. 2023;60(3).

27. DeSpirito J. Lateral jet interaction on a finned projectile in supersonic flow. Paper presented at: 50th Aerospace Sciences Meeting; 2012 Jan; Nashville, TN.

28. DeSpirito J. Transient lateral jet interaction effects on a generic fin-stabilized projectile. Paper presented at: 30th AIAA Applied Aerodynamics Conference; 2012 June; New Orleans, LA. AIAA Paper No.: 2012-2907.

29. Sahu J, Fresconi F, Heavey KR. Unsteady aerodynamic simulations of a finned projectile at a supersonic speed with jet interaction. Paper presented at: 32nd AIAA Applied Aerodynamics Conference; 2014 June; Atlanta, GA. AIAA Paper No.: 2014-3024.

30. Paul J, DeSpirito J, Sahu J. Computational investigation of control effectors on a generic high-speed vehicle. In: Proceedings of the AIAA SciTech 2024 Forum; 2024 Jan; Orlando, FL. AIAA SciTech Paper No.: 2024-2342.

31. Paul J, DeSpirito J, Sahu J. Computational investigation of control effectors on a generic high-speed vehicle. DEVCOM Army Research Laboratory (US); 2024 Sep. Report No.: ARL-TR-9979.

32. Bryson J, Vasile J, Gruenwald B, Fresconi F. Control surface design analysis and actuation requirements development for munitions. In: Proceedings of the AIAA SciTech 2020 Forum; 2020 Jan; Orlando, FL. AIAA SciTech 2020-0020.

33. Aftosmis MJ, Berger MJ, Adomavicius G. A parallel multilevel method for adaptively refined Cartesian grids with embedded boundaries. Paper presented at: 38th Aerospace Sciences Meeting and Exhibit; 2000; Reno, NV. AIAA Paper No.: 2000-0808.

34. Peroomian O, Chakravarthy S, Goldberg U. A ‘grid-transparent’ methodology for CFD. 1997. AIAA Paper No.: 97-07245.

35. Peroomian O, Chakravarthy S, Palaniswamy S, Goldberg U. Convergence acceleration for unified-grid formulation using preconditioned implicit relaxation. 1998. AIAA Paper No.: 98-0116.

36. Goldberg UC, Peroomian O, Chakravarthy S. A wall-distance-free K-E model with enhanced near-wall treatment. ASME J Fluids Eng. 1998;120:457–462.

37. Metacomp Technologies. MIME user's manual. Agoura Hills (CA): Metacomp Technologies (US); 2018.

Nomenclature

α	Angle of Attack
C_A	Axial Force Coefficient
C_s	Side Force Coefficient
C_N	Normal Force Coefficient
C_l	Roll Moment Coefficient
C_m	Pitching Moment Coefficient
C_n	Yawing Moment Coefficient
C_p	Surface Pressure Coefficient
ΔC_A	Axial Force Coefficient Increment Due to Pin Effectors
ΔC_m	Pitching Moment Coefficient Increment Due to Pin Effectors
ΔC_N	Normal Force Coefficient Increment Due to Pin Effectors
M	Mach Number

List of Symbols, Abbreviations, and Acronyms

3-D	Three-Dimensional
6DOF	Six Degrees-of-Freedom
ARL	Army Research Laboratory
CFD	Computational Fluid Dynamics
DEVCOM	U.S. Army Combat Capabilities Development Command
GTRI	Georgia Tech Research Institute
MIME	Multipurpose Intelligent Meshing Environment
NASA	National Aeronautics and Space Administration
RANS	Reynolds-Averaged Navier–Stokes
RBD	Rigid-Body Dynamics

1 (PDF)	DEFENSE TECHNICAL INFORMATION CTR DTIC OCA
1 (PDF)	DEVCOM ARL FCDD RLB CB TECH LIB